



Evaluation of ozone trends in the mesosphere/lower thermosphere using a new merged dataset of ozone profiles

Monika E. Szlag¹, Viktoria F. Sofieva¹, Edward Malina², Pekka T. Verronen^{1,3}, Michelle L. Santee⁴, Manuel López-Puertas⁵, Bernd Funke⁵, Gabriele Stiller⁶, Alexandra Laeng⁶, Kaley A. Walker⁷, Patrick E. Sheese⁷, Mark E. Hervig⁸, and Benjamin T. Marshall⁹

¹Finnish Meteorological Institute, Helsinki, Finland

²ESA/ESRIN, Frascati, Italy

³Sodankylä Geophysical Observatory, University of Oulu, Sodankylä, Finland

⁴Jet Propulsion Laboratory, California Institute of Technology, Pasadena, California, USA

⁵Instituto de Astrofísica de Andalucía, CSIC, Granada, Spain

⁶Karlsruhe Institute of Technology, Karlsruhe, Germany

⁷Department of Physics, University of Toronto, Toronto, Canada

⁸GATS, Driggs, Idaho, USA

⁹GATS, Hampton, Virginia, USA

Correspondence: Monika E. Szlag (monika.szlag@fmi.fi)

Received: 15 December 2025 – Discussion started: 18 December 2025

Revised: 10 March 2026 – Accepted: 16 March 2026 – Published: 29 May 2026

Abstract. In recent years, the need for high-quality long-term mesospheric ozone records has become increasingly evident, as they are essential for understanding chemical, dynamical, and radiative processes in the middle and upper atmosphere and their coupling with the lower layers. Here, we present a new merged dataset of ozone profiles in the middle atmosphere (METEOR-O3), created from several limb-viewing satellite instruments: HALOE, GOMOS, MIPAS, ACE-FTS, MLS, and SOFIE. The merged dataset covers the period from 1991 to 2023 and provides deseasonalized ozone anomalies in 10° latitude bins between 80° S and 80° N, from approximately 22 to 100 km. The deseasonalized ozone anomalies are used for global and seasonal trend analysis. The results show positive upper stratospheric ozone trends in both hemispheres, with magnitudes of 1 %–2 % per decade between 35 and 45 km, indicating continued ozone recovery consistent with previous assessments. In contrast, mesospheric ozone (above ~60 km) exhibits negative trends of –1 % to –3 % per decade, with the strongest decreases of about –8 % to –12 % per decade between 80 and 90 km. Seasonal analyses confirm positive trends in the upper stratosphere across all seasons and persistent negative trends in the upper mesosphere, strongest at high latitudes above 80 km. The METEOR-O3 dataset provides the first global, long-term merged record suitable for detailed studies of mesospheric/lower thermospheric ozone variability and trend evaluation, providing valuable information for model validation and assessments of upper atmospheric changes.

1 Introduction

Understanding long-term trends in the mesosphere and lower thermosphere (MLT, ~ 50 – 120 km) is becoming increasingly important as they can serve as a valuable indicator of climatic change. Trends in the MLT region exhibit significant variability, which can be influenced by solar activity, atmospheric dynamics, and anthropogenic factors (Laštovička, 2017, 2023, and references therein). Over the last few years, the upper atmosphere has been widely studied, particularly concerning long-term trends. While temperature remains the most extensively studied, other parameters (winds, water vapour, minor constituents) have been analysed as well (Laštovička, 2023; Cnossen et al., 2024, and reference therein).

The middle and upper atmosphere is experiencing a global mean negative temperature trend observed across datasets and models caused by the increasing concentration of CO_2 (Laštovička, 2006; Qian et al., 2021; Cnossen, 2020). Increases in CH_4 and H_2O , along with decreasing stratospheric O_3 , contribute to cooling in the stratosphere and mesosphere, but their influence becomes negligible in the upper thermosphere (Cnossen et al., 2024 and references therein). The mesospheric cooling trend has been observed in ground-based and satellite measurements with a magnitude of about 0.5 – 2 K per decade (Yuan et al., 2019; Bailey et al., 2021; Das, 2021; Li et al., 2021). Numerical simulations generally confirm the cooling trend except for the summer upper mesosphere, which shows near-zero or slightly positive temperature trends, likely reflecting dynamical effects (Qian et al., 2019; Solomon et al., 2019).

The long-term trends in dynamical processes, which are important in the MLT, are more complex. Observations and simulations reveal large spatial and temporal variability in wind trends, often differing between regions and seasons (Qian et al., 2019; Wilhelm et al., 2019). Research on atmospheric waves has been limited and concentrating mainly on tides (Laštovička, 2023). No significant long-term changes in diurnal tides have been observed, while semidiurnal components show mixed results that vary with altitude and latitude (Wilhelm et al., 2019). Overall, dynamical trends in the MLT are poorly constrained and regionally dependent, remaining a major source of uncertainty in understanding the MLT's long-term evolution (Laštovička, 2023 and references therein).

Mesospheric ozone plays an important role in atmospheric chemistry, dynamics, and energy balance, yet it remains one of the least-investigated parameters (Laštovička, 2023). Variations in its concentration can substantially influence the composition and behavior of the upper and middle atmosphere, thereby affecting the coupling between different atmospheric layers (Sinnhuber et al., 2012; Seppälä et al., 2009, 2025). In recent years, there has been a growing scientific interest in understanding solar-driven changes in ozone and temperature in the mesosphere and upper stratosphere (Salminen et al., 2019; Szelag et al., 2022; Seppälä et al.

2024). These variations, although occurring alongside the rapid climate change driven by anthropogenic greenhouse gas emissions, have the potential to regulate regional climate on annual to decadal timescales (Baumgaertner et al., 2011; Langematz et al., 2005; Maliniemi et al., 2014; Rozanov et al., 2005, 2012; Seppälä et al., 2009, 2013). Understanding these complex interactions between human-induced and naturally driven climate variability is particularly important in the polar regions, which are experiencing some of the most significant changes.

While individual satellite instruments provide ozone measurements in the mesosphere, their operation is limited in time. To date, a comprehensive merged data set combining multiple sources of mesospheric ozone data is not available, and an assessment of global mesospheric ozone trends has not been conducted. Previous analyses (Bizuneh et al., 2022; Huang et al., 2014; Nath and Sridharan, 2014) based on 10–15 years of SABER (Sounding of the Atmosphere using Broadband Emission Radiometry) data were confined to narrow latitude ranges (5 – 15° N) or limited to lower and middle latitudes (48° S– 48° N), thereby restricting insight into global long-term mesospheric ozone variability. Moreover, SABER ozone data are known to suffer from quality limitations (López-Puertas et al., 2023), underscoring the need for improved observational datasets and longer time series to establish reliable long-term trends.

In this paper, we introduce a new merged dataset of ozone profiles in the middle atmosphere, created using the data from several limb and occultation instruments: HALOE (Halogen Occultation Experiment), GOMOS (Global Ozone Monitoring by Occultation of Stars), MIPAS (Michelson Interferometer for Passive Atmospheric Sounding), ACE-FTS (Atmospheric Chemistry Experiment – Fourier Transform Spectrometer), MLS (Microwave Limb Sounder), and SOFIE (Solar Occultation For Ice Experiment). The paper is organized as follows. In Sect. 2, we provide short descriptions of the data used for the merged dataset. In Sect. 3, we describe the data preparation for the merging procedure, which is discussed in Sect. 4. Section 5 describes the new merged METEOR- O_3 dataset. Section 6 is dedicated to trends analyses in the upper atmosphere. The summary (Sect. 7) concludes the paper.

2 Data

For the merged dataset of ozone mixing ratio profiles, we used profiles from the limb and occultation instruments that provide ozone data in the mesosphere and the lower thermosphere: HALOE, GOMOS, MIPAS, ACE-FTS, MLS, and SOFIE, as described below. For several instruments, the data are from the HARMonized dataset of Ozone profiles (HARMOZ) collection (Sofieva et al., 2013).

2.1 HALOE

The Halogen Occultation Experiment (HALOE) was a solar occultation instrument that operated on board the Upper Atmosphere Research Satellite (UARS) from September 1991 until November 2005 (Russell et al., 1993). HALOE typically recorded about 15 sunrise and sunset events per day, between 3 and 130 km altitude, with a vertical resolution of about 2 km. HALOE was able to cover the entire latitude range from 80° S to 80° N within a time span of about two to six weeks, depending on the time of year.

Here we use Level 2 data obtained with the version 19 processing algorithm. Ozone observations were performed using a broadband spectral channel centered around 9.6 μm . The error estimates account for random noise and altitude-dependent quasi-systematic uncertainties, primarily arising from aerosol correction inaccuracies. These errors are about 5 %–10 % in the middle and upper atmosphere, increasing to around 30 % near the 100 hPa level (Bhatt et al., 1999).

2.2 GOMOS

The Global Ozone Monitoring by Occultation of Stars (GOMOS) was a stellar occultation instrument that operated on board Envisat (ENVironmental SATellite) over 2002–2012 (Bertaux et al., 2010; Kyrölä et al., 2010). Ozone profiles are retrieved from the ultraviolet (UV) and visible spectrometer measurements at wavelengths between 250 and 692 nm. The main dataset consists of nighttime ozone profiles with solar zenith angle larger than 105° (equatorial crossings at 10:00 p.m. local time), which are retrieved from atmospheric transmittance spectra. For this study, we use GOMOS ozone profiles obtained with the ALGOM2s v1.0 processor (Sofieva et al., 2017a). ALGOM2s is identical to the ESA IPF v6 processor in the stratosphere and MLT but has improved data quality in the upper troposphere/lower stratosphere (UTLS).

GOMOS provides stratospheric and MLT ozone profiles with a vertical resolution of 2 km below 30 km, 3 km above 30 km, with a linear transition between (Tamminen et al., 2010). The vertical resolution of the GOMOS ozone profiles is the same for all occultations due to the Tikhonov-type target-resolution regularization (Kyrölä et al., 2010; Sofieva et al., 2004). The stellar flux recorded by GOMOS, and thus signal-to-noise ratio and precision of retrieved profiles, depends on stellar magnitude and spectral class. The estimated random uncertainty of GOMOS ozone profiles in the MLT is 1 %–7 % (Tamminen et al., 2010).

GOMOS exploits a self-calibrating measurement principle, therefore high stability of the GOMOS data is expected (Kyrölä et al., 2010). It turned out that it is important to exclude the ozone data from the stars with insufficient UV-flux. In our study, we used the GOMOS data from the HARMOZ dataset, which consists of valid data only.

2.3 MIPAS

The Michelson Interferometer for Passive Atmospheric Sounding (MIPAS) was an infrared limb emission spectrometer that was flown on the Envisat platform (Fischer et al., 2008). In 2002–2004, the instrument operated at full spectral resolution. Due to a failure of the instrument's mirror slide in 2004, operations were suspended for almost 9 months and were resumed in January 2005 with reduced spectral but improved vertical resolution. These operations continued until the loss of communications with the ENVISAT platform in April 2012. Most of the time MIPAS observed the 6–68 km altitude range in its nominal mode (hereafter referred to as MIPAS_NOM). After 2005, it also pointed to higher altitudes less frequently (about one out of five days) in its middle atmosphere (MA, 20–102 km) and upper atmosphere (UA, 40–102 km) measurement modes (hereafter collectively referred to as MIPAS_MA_UA). The equator crossings occurred at approximately 10:00 a.m. and 10:00 p.m. local time.

Stratospheric ozone profiles are retrieved from MIPAS/ENVISAT limb emission spectra. In this work, we use version V8R_O3_261/561/661 ozone data derived with the scientific MIPAS level 2 processor developed by Karlsruhe Institute of Technology and Instituto de Astrofísica de Andalucía (IMK/IAA). The retrieval is performed via constrained inverse modelling of limb radiances. A detailed description can be found in von Clarmann et al. (2003, 2009). The data version used in this work is retrieved from new Level 1 spectra (version V8). Improvements in the Level 2 retrieval strategy are described in Kiefer et al. (2023), and López-Puertas et al. (2023) for the NOM and MA/UA modes, respectively.

Due to their different data characteristics, the two MIPAS measurement periods are usually treated as two independent datasets. Their processing schemes are different, and the vertical resolution of the early MIPAS period is lower than that of the later period: 5–8 km vs. 4–6 km for retrieved ozone in the mesosphere from MIPAS_NOM measurements. Therefore, and because of their short temporal coverage, data of the first measurement period (2002–2004) have not been considered in this study. The total random error in the mesosphere from MIPAS_NOM observations is on the order of 8 % (at 50 km) to 30 % (at 70 km), with a total systematic error in the same range. For MIPAS_MA_UA observations, the total random error ranges from 3 % at 50 km altitude to 20 %–30 % in the upper mesosphere/lower thermosphere, being larger in daytime than in nighttime. The total systematic error is rather constant over all altitudes and is in the range of 7 % to 10 %, including non-LTE (non-Local Thermodynamic Equilibrium) errors from uncertainties in the collisional and kinetic rate constants and the abundances of atmospheric species required for the non-LTE modelling (Kiefer et al., 2023; López-Puertas et al., 2023).

2.4 ACE-FTS

The Atmospheric Chemistry Experiment – Fourier Transform Spectrometer (ACE-FTS) on board the Canadian Science Satellite (SciSat) satellite (Bernath, 2017; Bernath et al., 2005) has been providing the data since February 2004 to present. It measures from about 85° N to 85° S with complete coverage every 3 months. The ACE-FTS is a high-spectral-resolution (0.02 cm^{-1}) Fourier transform spectrometer observing the 2.2–13 μm range (Bernath et al., 2005). Using solar occultation, it provides vertical profiles for over 30 atmospheric species.

For each occultation, the ACE-FTS retrieval algorithm determines volume mixing ratio profiles by applying a global non-linear least-squares fitting technique, matching observed spectra with those produced by a forward model. A full description of this retrieval processor can be found in Boone et al. (2005). The current version of the ACE-FTS data set used for HARMOZ is v5.2, as described in (Boone et al., 2023). For ozone, the retrieval uses 40 microwindows between 829 and 2673 cm^{-1} and accounts for 15 different interfering species and subsidiary isotopologues. The altitude range of the retrieved ozone profiles is about 5–95 km, with a vertical resolution of approximately 3–4 km.

The ACE-FTS dataset includes quality flags (Sheese et al., 2015). For HARMOZ, data points with flag values > 0 at a given altitude and any profiles with flags 4–6 were removed. A recent validation study (Sheese et al., 2022) found that v4.1 ACE-FTS ozone (the latest version for which validation has been performed) exhibits a bias relative to other instruments of approximately -1% to $+5\%$ in the lower stratosphere, $+2$ to $+9\%$ in the middle stratosphere, and up to about $+15\%$ in the upper stratosphere. The estimated precision of v4.1 ozone is $\sim 6\%$ – 10% between 20 and 45 km and $\sim 5\%$ – 10% above 45 km.

2.5 MLS

The Microwave Limb Sounder (MLS), launched as part of NASA's Aura mission in July 2004, measures millimeter- and submillimeter-wavelength thermal emission from the limb of Earth's atmosphere (Waters et al., 2006). The Aura MLS field of view points in the direction of orbital motion and vertically scans the limb in the orbit plane, providing approximately 3500 daily vertical profiles of 16 trace gases, temperature, geopotential height, relative humidity with respect to ice, and cloud ice water content and path spaced at ~ 165 km along the orbit track from 82° S to 82° N latitude on every orbit. Aura is in a sun-synchronous orbit with a 01:45 p.m. local time ascending equator-crossing time; thus, MLS samples a given latitude on either the ascending (mainly day) or descending (mainly night) portions of each orbit at the same local solar time.

Here we use version 5 Level 2 MLS ozone measurements. The MLS retrieval algorithms, which employ an optimal es-

timization approach, are “tomographic” in nature, exploiting information from multiple consecutive limb scans to simultaneously estimate the two-dimensional (along-track and vertical) state of the atmosphere over multiple Level 2 profiles (Livesey et al., 2006). The quality and resolution of the version 5 MLS data vary by product and with altitude. For ozone, the vertical resolution ranges from ~ 2.5 – 3 km in most of the stratosphere to 7 km at 0.001 hPa (Livesey et al., 2022). The single-profile precision degrades from 0.04 ppmv at 100 hPa to 0.1 ppmv at 10 hPa, 0.2 ppmv at 1 hPa, 1.1 ppmv at 0.01 hPa, and 3.4 ppmv at 0.001 hPa. However, precision is generally improved by averaging (with the precision of an average of N profiles being a factor of the square root of N times smaller than the precision of an individual profile). The systematic uncertainty of version 5 ozone data is in the range 0.1 to 0.3 ppmv (on average 7%–25%) over most of the stratosphere and mesosphere but increases to 0.9 ppmv ($\sim 30\%$) at 0.001 hPa (~ 95 km).

2.6 SOFIE

The Solar Occultation For Ice Experiment (SOFIE) operated on board NASA's Aeronomy of Ice in the Mesosphere (AIM) satellite from April 2007 until March 2023 (Russell et al., 2009). It conducted measurements across 16 spectral bands, covering wavelengths from 0.29 to 5.32 μm , and provided vertical profiles of temperature and key atmospheric constituents, including H₂O, O₃, CO₂, CH₄, and NO (Hervig et al., 2009a, 2009b; Marshall et al., 2011). The instrument covered high latitudes of about 65–85° in both hemispheres with a vertical resolution of about 1.6 km. SOFIE measured 15 sunrise and sunset events per day between about 20 km and 105 km (Das et al., 2023; Gordley et al., 2009a, b).

Here we use ozone data from SOFIE Level 2 processing (v1.3) (Gordley et al., 2009b). Ozone measurements are made using two broadband filters at 292 nm (roughly 50–105 km) and 330 nm (from the tropopause to 60 km), with the former located in a spectral region of strong absorption that offers increased sensitivity in the mesosphere. These profiles are then combined to form a continuous ozone dataset extending from approximately the tropopause to 105 km. Refraction and Rayleigh scattering are accounted for in the SOFIE forward model. Additional interference comes from stratospheric aerosols below ~ 35 km (currently not corrected) and polar mesospheric clouds near 80–90 km during polar summer (corrected using the 330 nm band). Ozone errors result from uncertainties in the observations or the forward model. The combined random and systematic uncertainty in the O₃ mixing ratio is 3.4%–6.5% over the altitude range 30–100 km (Das et al., 2023).

2.7 METEOR-O₃ Data Summary

Information on the individual datasets specifically included in METEOR-O₃ is summarized in Table 1. All datasets used

to create the merged dataset have a vertical resolution of approximately 2–7 km in the MLT. Ozone measurements from the various satellite instruments provide global coverage and were obtained at different local times. The time series of the number of available ozone profiles per month from each dataset is shown in Fig. 1. Note that for some datasets, the selected period is shorter than their full operational period; for example, MIPAS_NOM data are included starting from 2005, as in Sofieva et al. (2017b, 2023). For instruments measuring in different illumination conditions (for example, daytime and nighttime measurements by MLS and MIPAS_NOM), the number of profiles per month is nearly identical. Latitudinal coverage of some of the datasets is illustrated in the Supplement (Figs. S1 and S2). The best spatial coverage is provided by instruments with dense sampling (MLS and MIPAS_NOM), while solar occultation instruments contribute 14–15 sunrise and sunset measurements per day. SOFIE data are limited to the polar regions, and its sampling pattern changes around 2016 due to shifts in sunrise/sunset measurement geometry (Fig. S1). Consequently, for Southern Hemisphere high latitudes the SOFIE anomaly record extends only until 2016, whereas in the Northern Hemisphere it continues through 2023.

For GOMOS, MIPAS, and ACE-FTS, the data from the user-friendly HARMOZ (Sofieva et al., 2013) are used. HARMOZ consists of the original retrieved ozone profiles from each instrument, screened for invalid data by the instrument experts and presented on a common vertical grid and in a common netCDF4 format, which simplifies the data usage. Below are more detailed descriptions of the individual datasets.

3 Preparation and selection of data for merging

Since the data in the longest dataset with dense sampling, MLS, are retrieved on a pressure grid, pressure was selected as the vertical coordinate. HALOE ozone profiles are also retrieved on a pressure grid. MIPAS (both datasets), ACE-FTS and SOFIE ozone profiles are retrieved on a geometric altitude grid, but temperature and pressure profiles are also retrieved from the measurements, so the conversion to a pressure grid is straightforward. GOMOS provides ozone number density profiles on an altitude grid. Since the temperature and pressure profiles provided in the GOMOS files rely on a combination of ECMWF analyses and the MSIS90 model (Mass Spectrometer–Incoherent Scatter model; Hedin, 1983, 1991) and are therefore not very accurate, we used an altitude–pressure relationship derived from MIPAS_MA_UA measurements to convert the GOMOS profiles (registered in altitude) to a pressure grid. The GOMOS mixing ratios are computed consistently with the altitude–pressure–density conversion (see detailed description in the Supplement).

For creating monthly zonal-mean data from the individual datasets, 10° latitude bands from 80° S to 80° N are used.

The specific challenge for combining ozone data in the mesosphere is that measurements are made at different local times, while diurnal variations are large in the MLT. Therefore, we first computed monthly zonal-mean ozone profiles for each illumination condition: daytime (solar zenith angle < 90°), nighttime (solar zenith angle > 108°), sunset or sunrise. For MLS and MIPAS make daytime and nighttime measurements, HALOE, ACE-FTS and SOFIE measure at sunset and sunrise.

For all datasets, the monthly zonal average is computed as the mean of ozone profiles $x_k(t, z, \theta, l)$, for each illumination condition l (daytime, nighttime, sunset, sunrise), month t , pressure level z and latitude band θ :

$$\rho(t, z, \theta, l) = \frac{1}{N_t} \sum x_k(t, z, \theta, l), \quad (1)$$

where N_t is the number of measurements available in month t . We required $N_t > 10$ in computation of monthly zonal-mean values. The uncertainty of the monthly mean $\sigma_\rho^2(t, z, \theta, l)$ can be estimated as the standard error of the mean:

$$\sigma_\rho^2(t, z, \theta, l) = \frac{s^2(t, z, \theta, l)}{N_t}, \quad (2)$$

where $s^2(t, z, \theta, l)$ is the sample variance. In Eq. (2), we used a robust estimator for the sample variance, i.e., $s = 0.5(P_{84} - P_{16})$, where P_{84} and P_{16} are the 84th and 16th percentiles of the distribution, respectively, similarly to the approach taken by Sofieva et al. (2017b).

To assess dataset consistency prior to merging, Figs. 2–3 demonstrate how well the various individual datasets reproduce the vertical structure and diurnal behaviour of ozone in the stratosphere and MLT. The monthly zonal-mean boreal wintertime (DJF) ozone distributions for MLS, MIPAS_NOM, MIPAS_MA_UA and GOMOS are presented in Fig. 2. The averaged values were calculated for the period 2005–2011 for these datasets. This period was chosen for intercomparison purposes, as it represents a time window with overlapping observations from MLS, MIPAS_NOM, MIPAS_MA_UA, and GOMOS. The top panel shows nighttime conditions, while the bottom panel represents daytime. Pressure altitudes are computed from pressure as $z = 16 \log_{10}(1013/P)$, where P is pressure in hPa. This pressure-derived altitude coordinate is used throughout the manuscript.

Across datasets, ozone distributions are similar, highlighting well-defined features. The nighttime ozone vertical distribution (top panels in Fig. 2) exhibits three distinct maxima. The primary ozone maximum occurs in the stratosphere, between approximately 30 and 35 km, where ozone mixing ratios reach about 10–11 ppmv (maximum in the tropics). It is produced through a photochemical equilibrium involving oxygen molecules, atomic oxygen, and solar ultraviolet radiation, and is modulated by natural variability and human activities (e.g. ozone-depleting substances, NO_x cycle;

Table 1. Description of datasets included in the METEOR-O₃.

Dataset name	Satellite/processor	Time period	Illumination conditions	Vertical range/retrieval coordinate	Vertical resolution	Latitude coverage
HALOE	UARS/v19	Sep 1991–Nov 2005	sunrise sunset	~45–0.001 hPa*, pressure	~2 km	~ monthly global
GOMOS	ENVISAT/ALGOM 2s v1	Aug 2002–Dec 2011	nighttime	~22–100 km, altitude	3 km	~ weekly global
MIPAS_NOM	Envisat KIT/IAA v8	Jan 2005–Apr 2012	daytime nighttime	~22–70 km, altitude	~3–5 km	daily global
MIPAS_MA_UA	Envisat KIT/IAA v8	Jan 2005–Apr 2012	daytime nighttime	~22–100 km, altitude	~3–5 km	daily global
ACE-FTS	SCISAT/v5.2	Feb 2004–Dec 2023	sunrise sunset	~22–95 km, altitude	~3–4 km	~ monthly global, best at mid-latitudes
MLS	Aura/NASA v5	Aug 2004–Dec 2023	daytime nighttime	~45–0.001 hPa*, pressure	~3–7 km	daily global
SOFIE	AIM/v1.3	Apr 2007–Mar 2023	sunrise sunset	~35–100 km, altitude	~2 km	high latitudes (65–85°)

* Corresponding to ~22–95 km altitude



Figure 1. Monthly data volume (logarithm of number of measurements) at 60 km. Top panel: nighttime/sunset measurements, bottom panel: daytime/sunrise measurements.

Brasseur and Solomon, 2005). The secondary maximum is found around 90–95 km, with the nighttime values as high as the stratospheric maxima (~10 ppmv). The secondary ozone peak represents a short-lived photochemical equilibrium strongly influenced by temperature and by the concentrations of atomic hydrogen and atomic oxygen (Smith and Marsh, 2005). During polar winter, a tertiary ozone maximum of roughly 2–3 ppmv develops near 72 km, peaking

close to the polar night terminator. This feature results from reduced concentrations of odd hydrogen during nighttime, decreasing odd-oxygen losses via HO_x catalytic cycles (e.g., Marsh et al., 2001; Sofieva et al., 2009).

In the middle and lower stratosphere, ozone exhibits relatively small diurnal variations because atomic oxygen concentrations are small compared to ozone, and ozone lifetimes exceed one day. As altitude increases into the MLT, diur-

nal variations become stronger. They are mainly controlled by the daytime photolysis of ozone and its reformation at night through the recombination of atomic and molecular oxygen. The efficiency of ozone production increases with altitude as atomic oxygen becomes more abundant (Brasseur and Solomon, 2005).

Figure 3 presents the monthly zonal-mean ozone distributions for boreal winter (DJF) as measured by the occultation instruments ACE-FTS, HALOE, and SOFIE. The DJF means were calculated for the periods 2005–2011 for ACE-FTS, 1991–2005 for HALOE, and 2007–2023 for SOFIE. Selecting 2005–2011 as the common period (as done for the limb measurements) is not possible here, because the time spans of the solar occultation instruments differ. Only ACE-FTS overlaps with this period, whereas HALOE and SOFIE operate largely outside it. Therefore, HALOE and SOFIE climatologies are shown for their full available periods, while ACE-FTS is presented for 2005–2011, consistent with Fig. 2. For the most part, similar features are observed as in Fig. 2. The ozone distributions show good consistency among all datasets, with spatial patterns clearly observed. However, a key difference is the nighttime ozone enhancement above 70 km. Solar occultation observations are limited to periods when the sun is rising or setting, rather than during complete darkness. The pronounced nighttime ozone enhancement in the MLT occurs during full darkness, outside the observation window of solar occultation instruments. The wintertime means from ACE-FTS and HALOE are in good agreement with those previously reported by Smith et al. (2013).

An example time series of nighttime ozone at northern mid-latitudes (30–60° N) from four instruments (MLS, MIPAS_NOM, MIPAS_MA_UA, and GOMOS), illustrating the vertical distribution of ozone over time, is shown in Supplement Fig. S4. Temporal variations in ozone are similarly represented across datasets, with key patterns over time clearly visible. Seasonal variations in ozone primarily manifest as an annual cycle in the stratosphere, with a maximum of about 10–11 ppmv in late spring/early summer. In the MLT region, a semi-annual cycle is observed, with ozone peaks of about 10–12 ppmv occurring around March–May and September–November.

4 The merging procedure

The merging procedure in general is like that used by Sofieva et al. (2017b, 2023) but is adapted for the MLT region by considering the strong diurnal cycle of ozone. Below we present the details of the merging procedure. It consists of three main steps: (i) evaluation of deseasonalized anomalies, (ii) data pre-merging, and (iii) final merging of pre-merged datasets from individual datasets.

4.1 Seasonal cycle and deseasonalized anomalies

For each dataset, illumination condition l , latitude band θ , and pressure level z , the climatological monthly mean ozone mixing ratio $\rho_m(z, \theta)$ (seasonal cycle) is first evaluated. The seasonal cycle is obtained by averaging the monthly zonal mean ozone mixing ratios over a set of selected years for a given month m :

$$\rho_m(z, \theta, l) = \frac{1}{N_m} \sum_{j=1}^{N_m} \rho_j(z, \theta, l), \quad (3)$$

where $\rho_j(z, \theta, l)$ is the monthly zonal mean ozone mixing ratio for month m in year j , and N_m is the number of selected years. For GOMOS, MIPAS_NOM, MIPAS_MA_UA, and MLS, the seasonal cycle is evaluated over the common operational period 2005–2011, ensuring consistency in the computation of median deseasonalized anomalies and avoiding biases arising from the use of different reference periods. For ACE-FTS, the seasonal cycle is derived from 2005–2018 to reduce sampling-related uncertainty, assuming negligible differences between the 2005–2011 and 2005–2018 seasonal climatologies. For HALOE and SOFIE, the full operational periods are used to estimate the seasonal cycle, and their deseasonalized anomalies are adjusted to the 2005–2011 reference period during merging (see below). The uncertainty of the seasonal cycle $\rho_m(z, \theta, l)$ for each month m , expressed as its variance $\sigma_m^2(z, \theta, l)$ is evaluated from uncertainties of individual monthly mean values $\sigma_{\rho,j}^2$ as

$$\sigma_m^2(z, \theta, l) = \frac{1}{N_m^2} \sum_{j=1}^{N_m} \sigma_{\rho,j}^2(z, \theta, l), \quad (4)$$

where $\sigma_{\rho,j}^2(z, \theta, l)$ is the variance of the monthly zonal mean ozone mixing ratio for month m in year j at altitude z and illumination condition l .

Figure 4 illustrates the climatological monthly mean $\rho_m(z, \theta, l)$ of nighttime ozone measurements for different latitude bands: 60–90° N, 30–60° N, 20° S–20° N, 30–60° S, and 60–90° S (from top to bottom), across four altitude ranges: 50–60, 60–70, 70–80, and 80–90 km (from left to right). The semi-annual cycle in the MLT is clearly visible, with ozone concentrations exhibiting two peaks per year during equinoxes.

Agreement among datasets is generally good, though some discrepancies between them exist, consistent with earlier validation and intercomparison results (Smith et al., 2013; López-Puertas et al., 2023; Das et al., 2023). Additionally, GOMOS shows some biases, which can be (partially) attributed to its coarser temporal and horizontal sampling, compared to that of MLS and MIPAS (see Fig. 1 and Sect. 2.2).

After evaluating the seasonal cycle, the deseasonalized ozone anomalies are computed as:

$$\Delta(t, z, \theta, l) = \frac{\rho(t, z, \theta, l) - \rho_m(z, \theta, l)}{\rho_m(z, \theta, l)}, \quad (5)$$

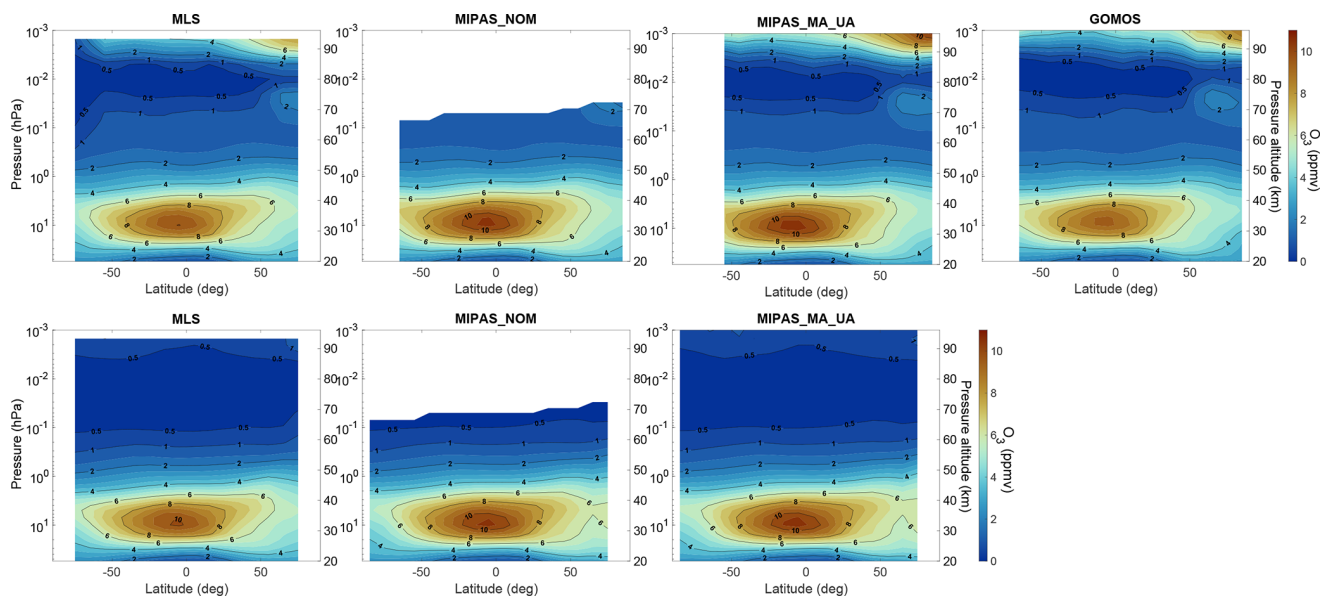


Figure 2. Boreal wintertime (DJF) zonal-mean ozone profiles for the years 2005–2011 for MLS, MIPAS_NOM, MIPAS_MA_UA and GOMOS (from left to right) for nighttime (top) and daytime (bottom) measurements.

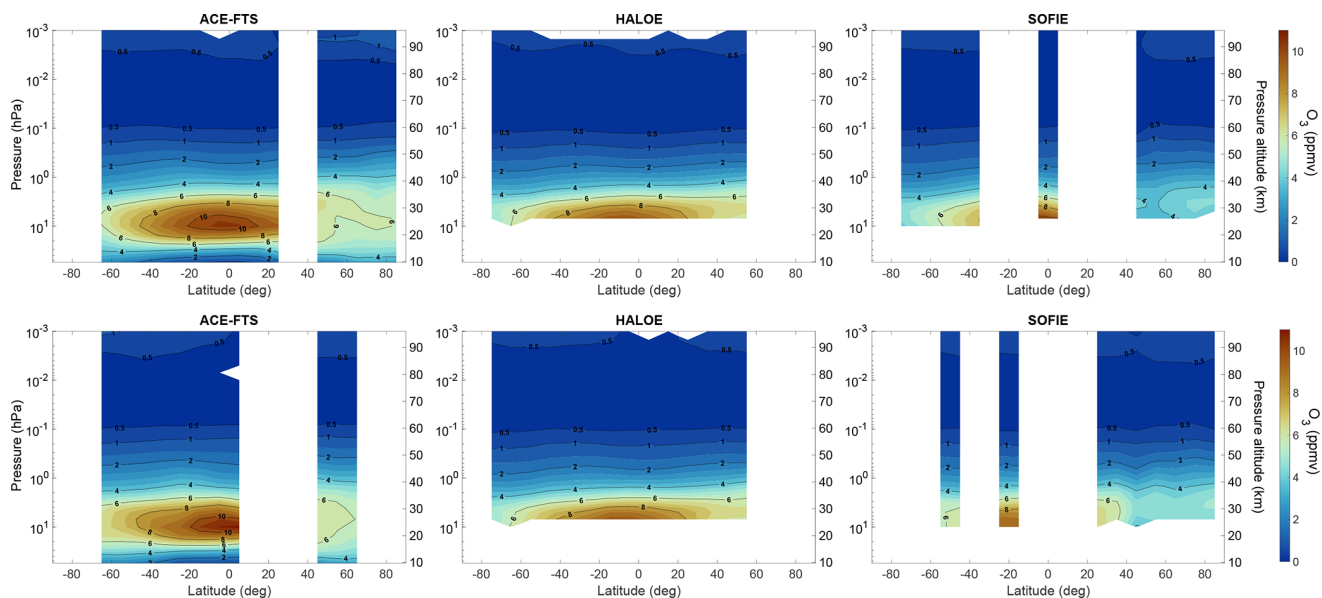


Figure 3. Boreal wintertime (DJF) zonal-mean ozone profiles for the years 2005–2011 for ACE-FTS, 1991–2005 for HALOE and 2007–2023 for SOFIE (from left to right) for sunset (top) and sunrise (bottom) measurements.

where $\Delta(t, z, \theta, l)$ is the monthly zonal mean ozone mixing ratio at month t , latitude band θ , illumination condition l and pressure level z (defined in Eq. 1), and $\rho_m(z, \theta, l)$ is the climatological monthly mean (seasonal cycle) for the corresponding month m (defined in Eq. 3). The uncertainty of the deseasonalized anomalies is evaluated using standard error propagation for each dataset, illumination condition and latitude band.

4.2 Pre-merging

Ozone in the mesosphere exhibits strong diurnal variations, as discussed above and illustrated in Figs. 2 and 3. This behaviour is also evident in the top panel of Fig. 5, which shows examples of absolute ozone mixing ratios from MIPAS_MA_UA at 56 km and 5° latitude under different illumination conditions l . While the absolute ozone mixing ratios differ substantially between illumination conditions, the deseasonalized anomalies (bottom panel of Fig. 5) are nearly

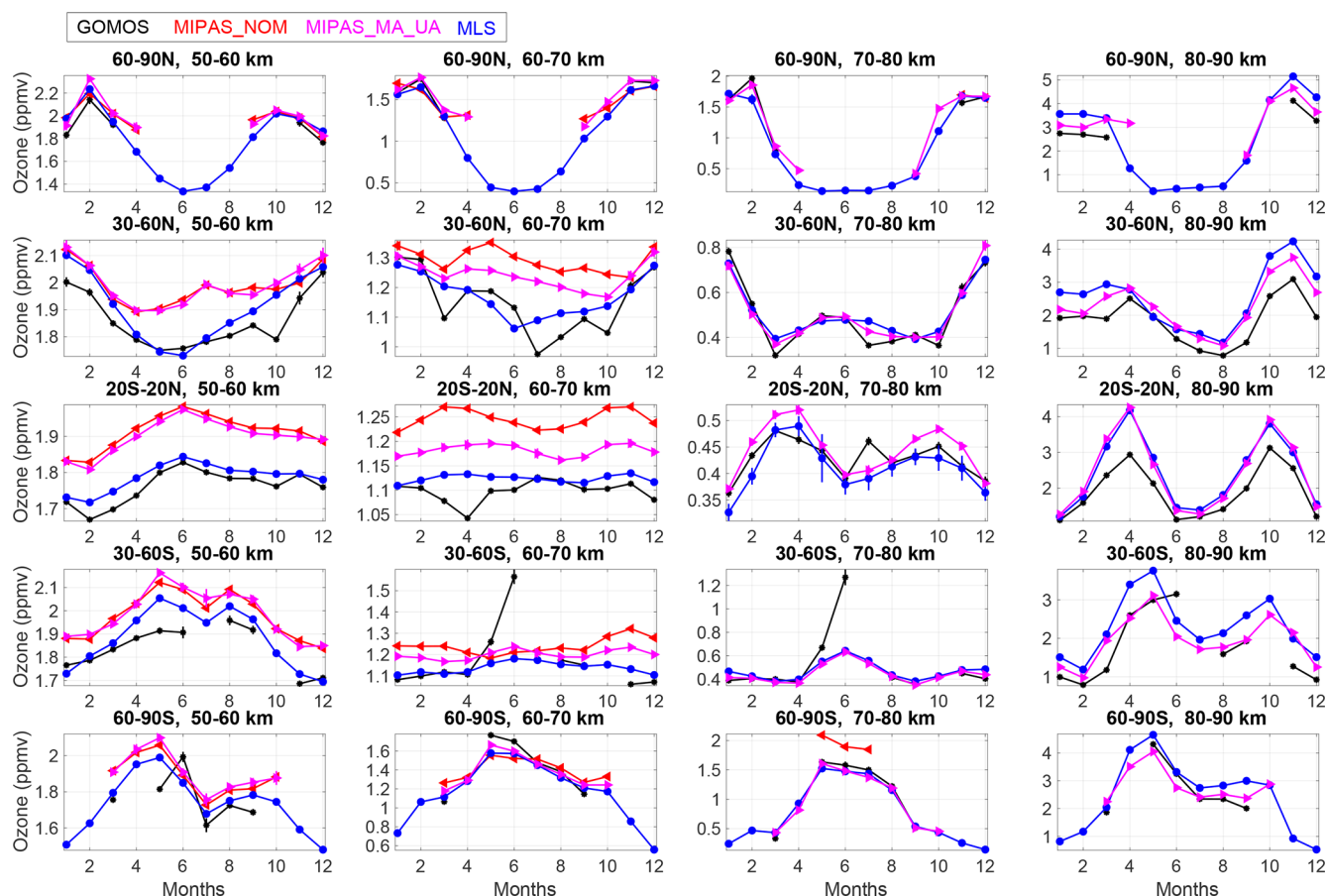


Figure 4. Ozone climatological monthly mean $\rho_m(z, \theta, l)$ of nighttime measurements in latitude bands 60–90° N, 30–60° N, 20° S–20° N, 30–60° S and 60–90° S (from top to bottom) for altitudes 50–60, 60–70, 70–80 and 80–90 km (from left to right). The seasonal cycles in the indicated zones are computed as the mean of seasonal cycles in 10° latitude bands.

identical for the instruments with dense sampling. The daytime, nighttime, and weighted mean deseasonalized anomalies are highly consistent across the full altitude range of the MIPAS_MA_UA measurements, as shown in Supplement Fig. S5. This validation procedure was performed across all datasets. Because the daytime and nighttime deseasonalized anomalies are nearly identical, we combine them by taking a weighted mean, which we refer to hereafter as “pre-merged” deseasonalized anomaly from each dataset. The weights are inversely proportional to the estimated uncertainties of the deseasonalized anomalies.

4.3 The merging procedure

The merging procedure is like that used for the SAGE-CCI-OMPS+ merged dataset (Sofieva et al., 2017b, 2023), and is illustrated in Fig. 6. First, we computed the merged anomaly as the median of all individual dataset anomalies, excluding HALOE and SOFIE, for each pressure level z , latitude band θ , and month t :

$$\Delta_{\text{merged}}(t, z, \theta) = \text{median}(\Delta_k(t, z, \theta)), \quad (6)$$

where $\Delta_k(t, z, \theta)$ indicates the individual dataset anomaly (top panel of Fig. 6). Next, the pre-merged HALOE and SOFIE anomalies, for which the seasonal cycles are calculated over different time periods (as explained above), are adjusted (offset) to this median anomaly. These offsets are generally very small (bottom panel of Fig. 6). Finally, the median of all aligned anomalies is computed (shown as red dots in the top panel of Fig. 6). The merging procedure is performed for each month, each latitude band, and each pressure level. An example of vertical profiles of pre-merged deseasonalized anomalies from individual datasets and the merged anomaly is shown in Fig. 7 for the latitude zone 60–70° S. The altitude coverage slightly varies between the datasets. The best spatio-temporal coverage is attained after 2004.

When performing data merging, we also analysed the deviations of individual pre-merged anomalies from the merged anomaly, to detect drifts or strong deviations. Such a comparison is shown in Fig. 8. No clear drifts were observed; the pre-merged anomalies from different datasets are in good agreement with each other.

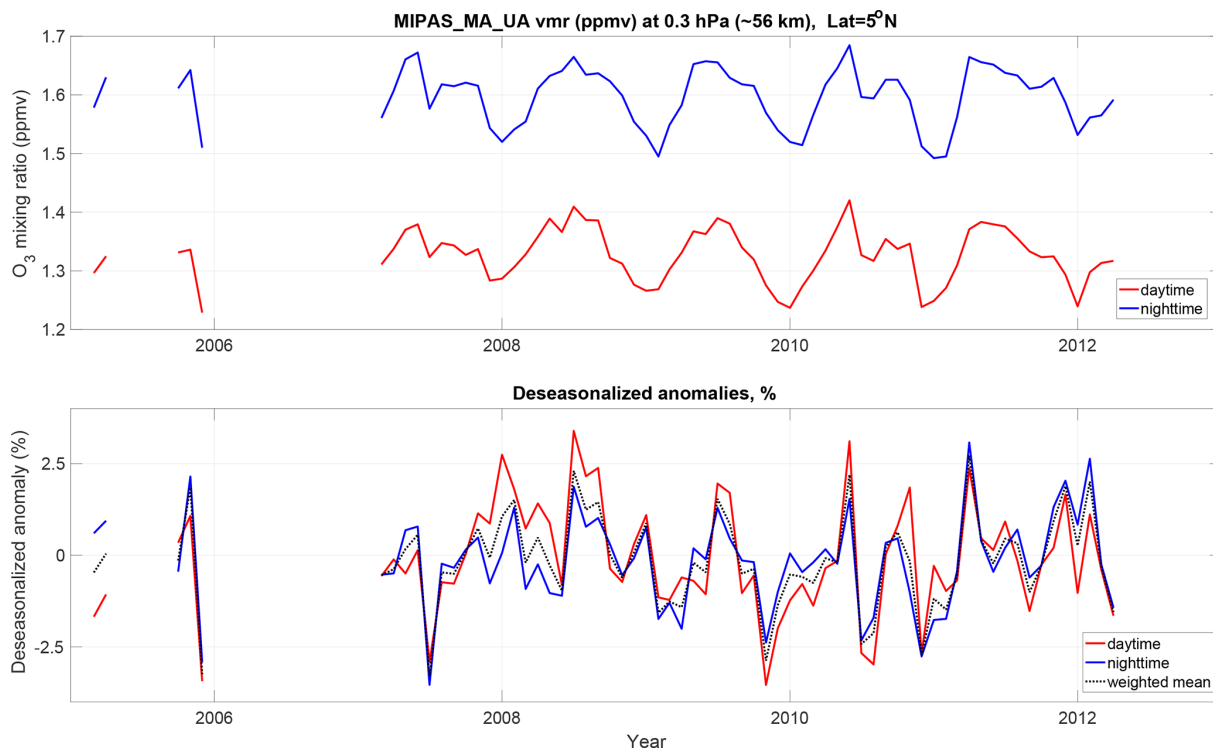


Figure 5. Top: ozone mixing ratio at 56 km for MIPAS_MA_UA daytime and nighttime observations in latitude zone 0–10° N. Bottom: the corresponding deseasonalized anomalies and the weighted mean anomaly (see text for explanation).

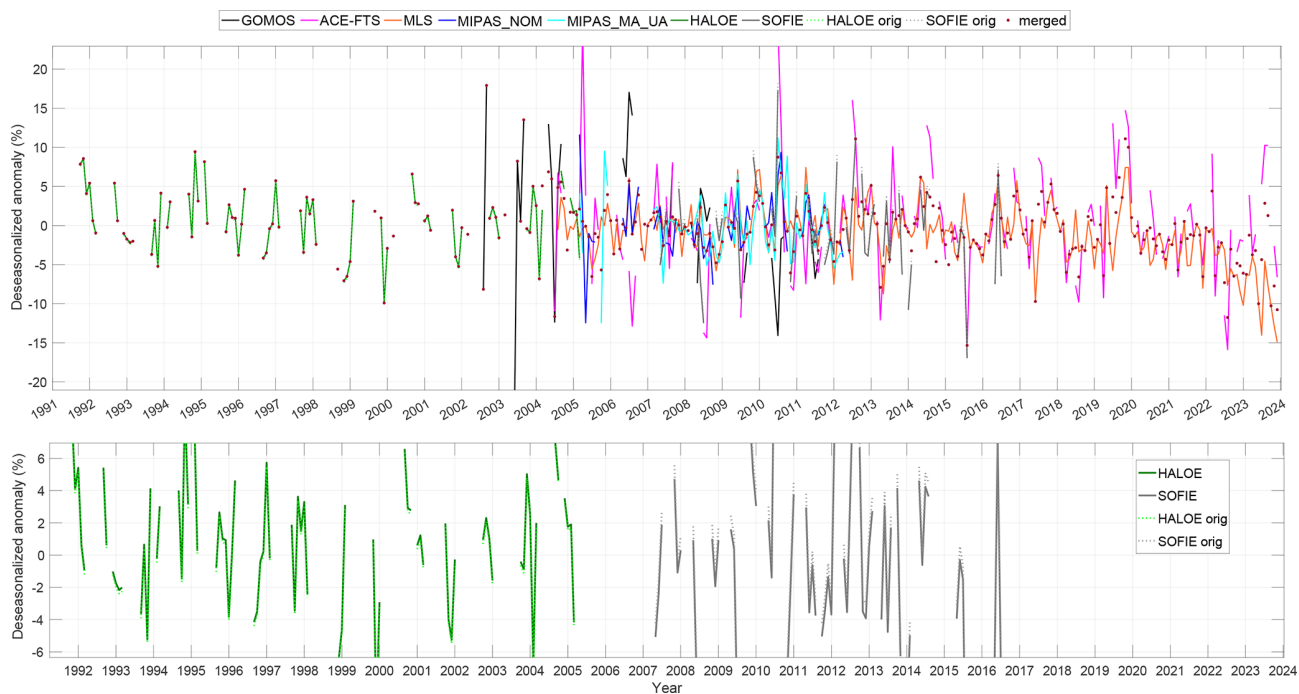


Figure 6. Illustration of the merging procedure using the data at 60–70° S, 0.05 hPa. Colored lines: individual pre-merged deseasonalized anomalies for different datasets (see legend). For HALOE and SOFIE, the original anomalies are shown by dotted lines, while offset anomalies are shown by solid lines. The final merged anomaly is shown by dark red dots. Top: all data, bottom: a zoom on HALOE and SOFIE anomalies for visualization of small offsets.

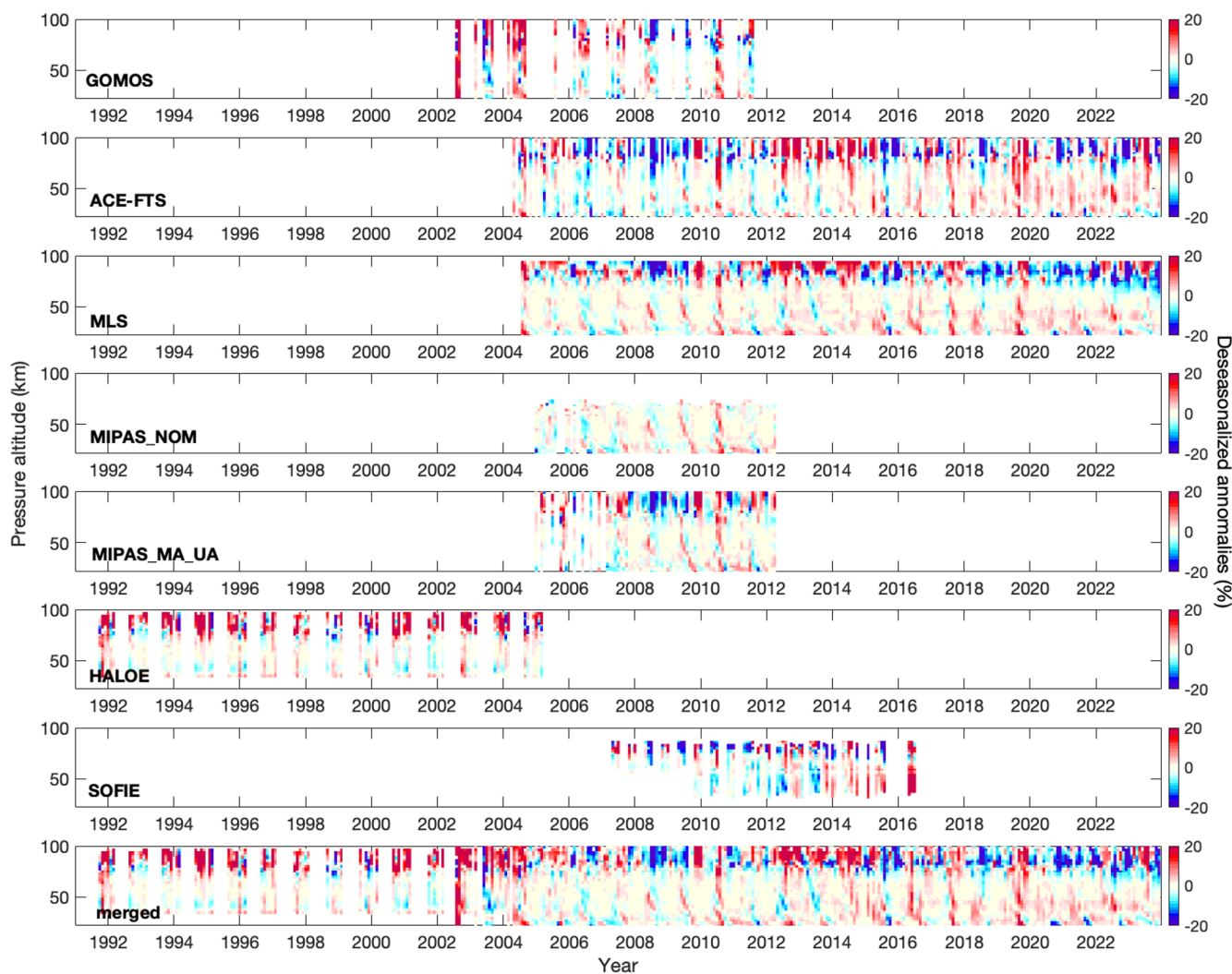


Figure 7. An example of vertical profiles of pre-merged deseasonalized anomalies from individual datasets and the final merged anomaly. The data are from the latitude zone 60–70° S.

The uncertainties of the merged ozone anomalies are evaluated as proposed by Sofieva et al., (2017b, 2023):

$$\sigma_{\Delta, \text{merged}}(t, z, \theta) = \min \left(\sigma_{\Delta, j_{\text{med}}}(t, z, \theta), \sqrt{\frac{1}{N} \sum_{j=1}^N \sigma_{\Delta, j}^2(t, z, \theta)} + \frac{1}{N^2} \sum_{j=1}^N (\Delta_j(t, z, \theta) - \Delta_{\text{merged}}(t, z, \theta))^2 \right), \quad (7)$$

where $\sigma_{\Delta, j_{\text{med}}}(t, z, \theta)$ is the anomaly uncertainty of the dataset corresponding to the median value. The typical uncertainties of the merged deseasonalized anomalies are shown in Fig. 9 for several latitude bins. In general, the estimated uncertainties are below 2%, except in the mesopause region, where they increase to 5%–10%. Before 2002, when the merged record consists solely of HALOE measurements,

the estimated uncertainties above 75 km are 5%–10% and < 2% below 70 km.

5 The merged METEOR-O₃ dataset of ozone profiles

The deseasonalized anomalies can be directly used for ozone trend analyses. For other applications, we also created merged ozone mixing ratio profiles. For this purpose, we computed the merged seasonal cycle as the mean of seasonal cycles from MLS, MIPAS_NOM and MIPAS_MA_UA, for daytime and nighttime illumination conditions. These datasets were selected because of their dense sampling, and to ensure maximum spatial coverage. A similar approach is applied for the merged stratospheric ozone datasets (Sofieva et al., 2017b, 2023). This merged seasonal cycle is then applied to the merged deseasonalized anomalies. Thus, in addition to deseasonalized anomalies, nighttime and daytime

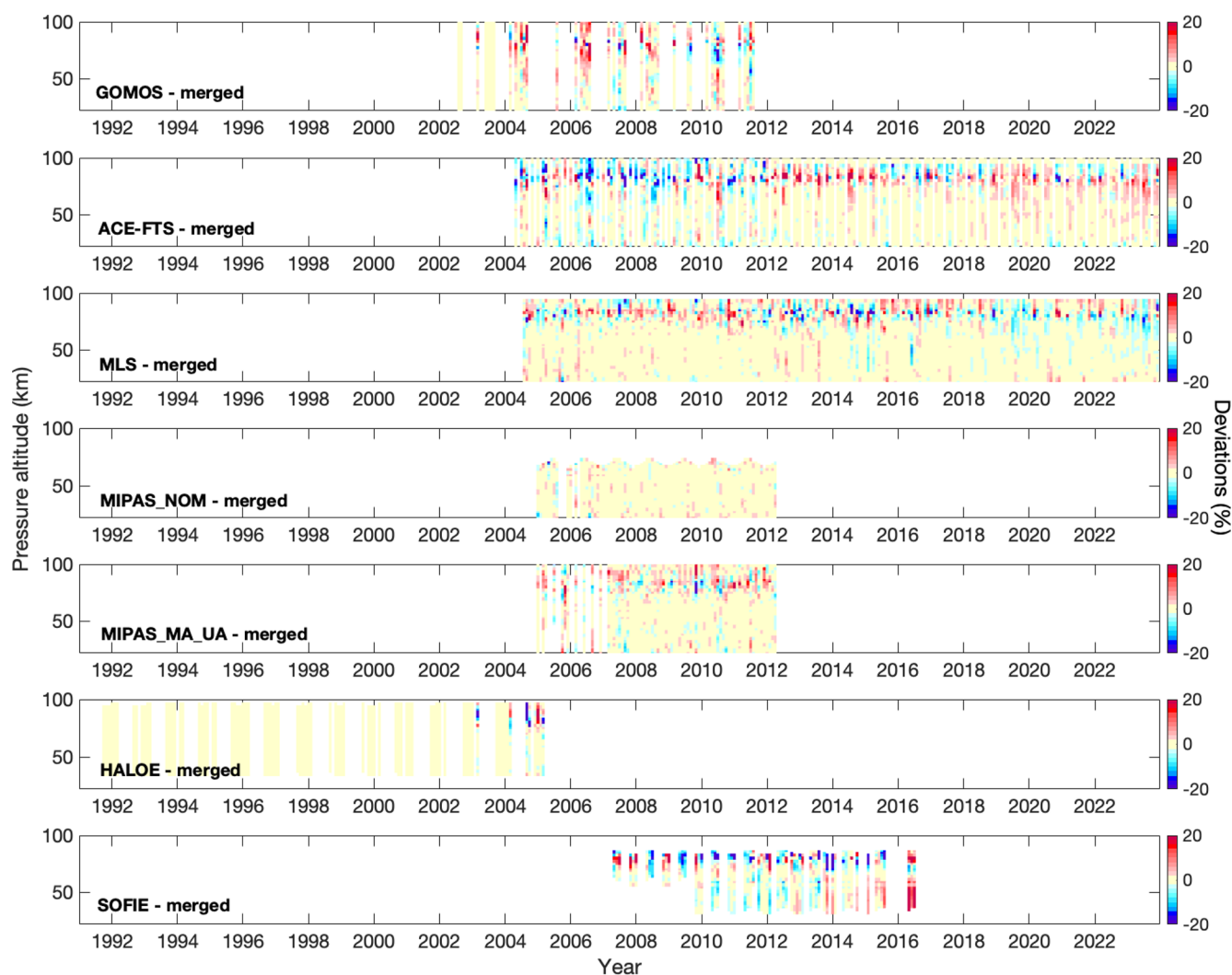


Figure 8. Example of deviations of individual deseasonalized anomalies from the merged anomaly. The data are from the latitude zone 60–70° S.

ozone mixing ratio profiles and their uncertainty are provided in the merged dataset. Examples of the merged METEOR- O_3 mixing ratio profiles are shown in Fig. 10.

6 Analyses of trends in the upper atmosphere

The merged deseasonalized ozone anomalies are suitable for direct use in ozone trend assessments. For this analysis, we apply a multiple linear regression (MLR) to the METEOR- O_3 dataset:

$$O_3(t) = \text{PWL}(t, t_0) + q_1 \text{QBO}_{30}(t) + q_2 \text{QBO}_{50}(t) + s F_{10.7}(t) + d \text{ENSO}(t), \quad (8)$$

where $\text{PWL}(t, t_0)$ is a piecewise linear term (constant and a hockey-stick trend with the turnaround point in 1997), $\text{QBO}_{30}(t)$ and $\text{QBO}_{50}(t)$ are two quasi-biennial oscillation (QBO) proxies (30 and 50 hPa equatorial winds; [http://](http://www.cpc.ncep.noaa.gov/data/indices/)

www.cpc.ncep.noaa.gov/data/indices/, last access: 12 May 2026), $F_{10.7}(t)$ is the monthly average solar 10.7 cm radio flux (<https://www.spaceweather.gc.ca/forecast-previous/solar-solaire/solarflux/sx-5-en.php>, last access: 12 May 2026), and $\text{ENSO}(t)$ is the 2-month lagged El Niño–Southern Oscillation (ENSO) proxy (<https://www.esrl.noaa.gov/psd/enso/mei/data/meiv2.data>, last access: 12 May 2026). The piecewise linear trend approach is motivated by the well-established ozone turnaround around in 1997 following the peak in ozone-depleting substances, which marks the recovery period (Harris et al., 2008). Similar formulations have been used in previous ozone trend studies (e.g., Bourassa et al., 2014; Kyrölä et al., 2013; Sofieva et al., 2017b). Uncertainties are derived from the residuals of the regression fits, and autocorrelation is corrected in both steps using the Cochrane-Orcutt transformation (Cochrane and Orcutt, 1949). Trends prior to 1997 are not shown because the

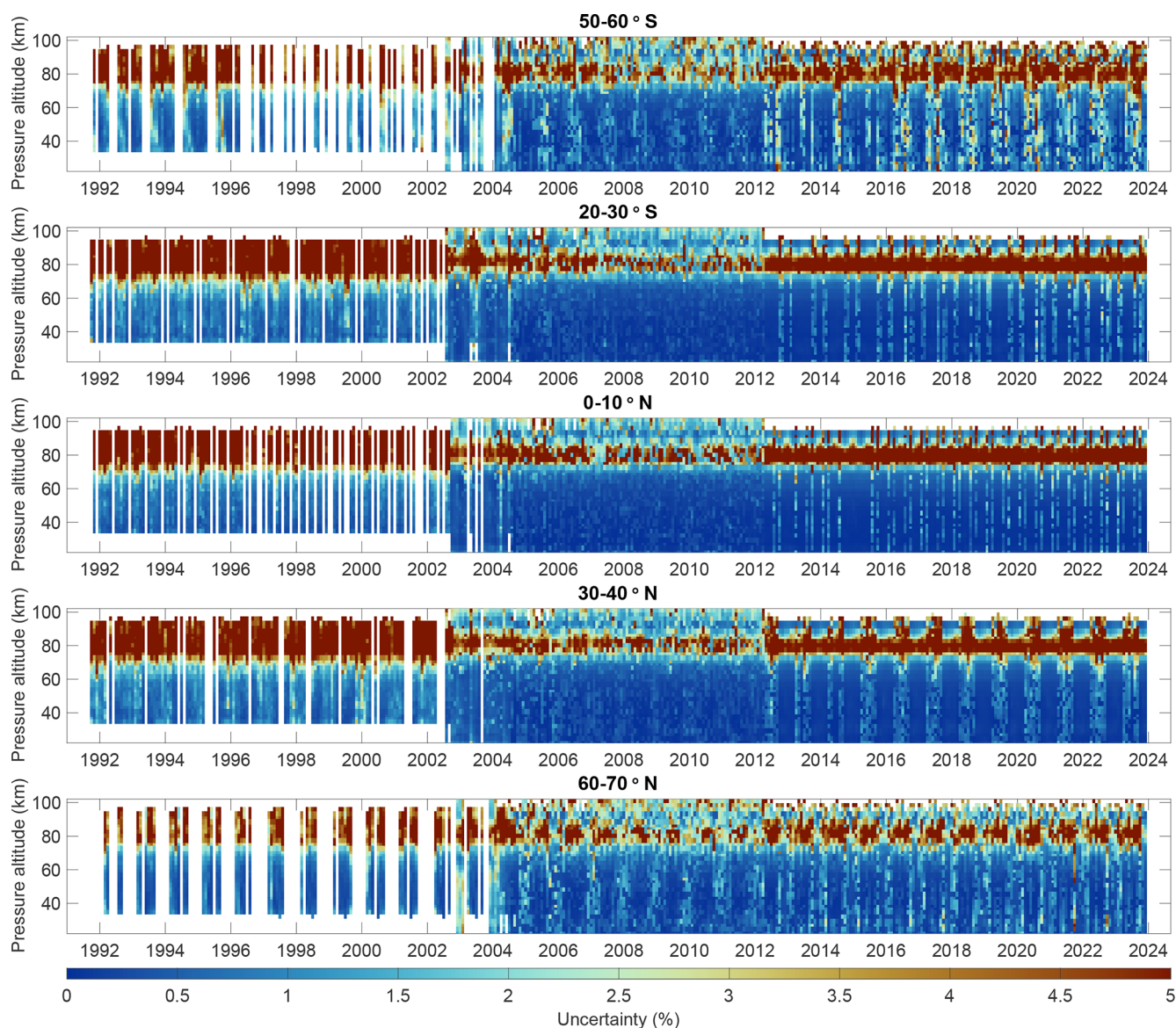


Figure 9. Examples of uncertainties (in %) of the merged deseasonalized anomalies. The latitude bins are indicated in the panels.

available record (1991–1996) is too short for a robust estimation of ozone trends, particularly given the strong interannual variability in mesospheric ozone.

For comparison, the regression analysis was performed in two ways. In the first approach, the MLR was applied to the entire merged dataset covering the period 1991–2023. In this case, the bottom altitude range was limited to the coverage of HALOE observations, starting at approximately 37 km and running up to 93 km. In the second approach, the MLR was applied only to the period with the best spatio-temporal coverage (2004–2023), extending from about 22 km upward. Since trend estimates can be sensitive to the choice of regression period (Harris et al., 2015), this approach also serves as a robustness test with respect to the selected analysis window.

Figure 11 shows the trend results for the stratospheric ozone recovery period (1997–2023) and for the best spatio-temporal coverage period (2004–2023). The trends are very similar for both considered periods. Stratospheric ozone trends are in very good agreement with previous ozone assessments (Godin-Beekmann et al., 2022; Petropavlovskikh et al., 2019). The results indicate continued recovery of ozone in the upper stratosphere, with positive values of about 1 %–2 % per decade between 35 and 45 km (above the primary ozone maximum) that are particularly pronounced at middle and high latitudes in both hemispheres.

In contrast, MLT ozone exhibits negative trends, reaching about -1% to -3% per decade over 60–80 km. The strongest decreases, of approximately -8% to -12% per decade, occur between 80 and 90 km, below the secondary

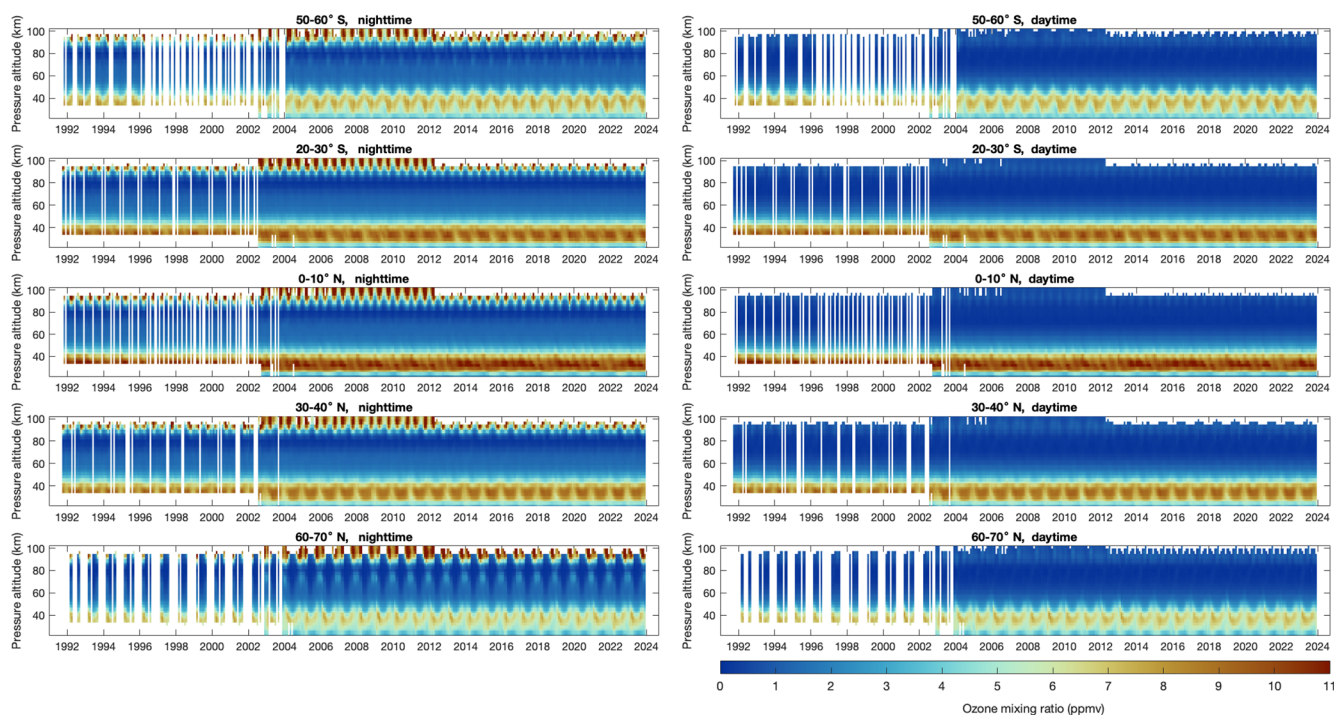


Figure 10. Examples of the merged METEOR- O_3 nighttime (left) and daytime (right) time series of ozone mixing ratio profiles. The latitude bins are indicated in the panels.

ozone maximum. Because the trends are expressed in percent, regions with lower background ozone can exhibit larger relative changes. Previous analysis based on 10 years (2002–2012) of SABER data confined to lower and middle latitudes (48°S – 48°N) revealed a marginally positive not-significant ozone trend at altitudes of 60–80 km and a strong negative trend up to -10% per decade near 85–100 km. Positive/negative ozone trends were accompanied by a cooling trend of about -3 K per decade (Huang et al., 2014). Regionally, Bizuneh et al. (2022), using 16 years of SABER data over low latitudes (5 – 15°N), have shown negative temperature and ozone trends (-0.85 K per decade and -0.12 ppmv per decade) in the lower mesosphere (60–80 km) but positive trends (1.25 K per decade and 0.27 ppmv per decade) in the upper mesosphere/lower thermosphere (85–100 km). Alongside natural drivers, the authors attributed these patterns to the influence of increasing greenhouse gas concentrations. Furthermore, rising H_2O levels in the mesosphere and lower thermosphere can enhance HO_x production, which accelerates ozone loss and may further contribute to the observed negative O_3 trends.

To assess sensitivity to the trend formulation, additional regressions were performed using the Long-term Ozone Trends and Uncertainties in the Stratosphere (LOTUS) regression model (<https://usask-arg.github.io/lotus-regression/>, last access: 12 May 2026) with an independent linear term (ILT). The ILT includes two linear terms: a pre-1997 trend and a post-2000 trend. Separate in-

tercepts allow the two periods to vary independently. In contrast, the PWLT predictors impose a common turnaround value in 1997. The resulting ozone trend patterns and magnitudes closely match those obtained with the original MLR (Supplement Fig. S6), demonstrating that, as with the trend period, the results are also not sensitive to the chosen trend representation.

In addition to the relative (% per decade) analysis, we have also derived trends based on absolute (ppmv) ozone values (Fig. 12). These trends are predominantly negative between 60 and 90 km, in qualitative agreement with regional studies (Bizuneh et al., 2022). In the 60–80 km range, trends vary from about -0.01 to -0.02 ppmv per decade during nighttime. At altitudes above 80 km, negative trends of about -0.15 to -0.2 ppmv per decade are observed, with the peak decreases occurring close to the secondary ozone maximum during nighttime. At northern mid-latitudes above 90 km, the trends weaken and in some regions transition to slightly positive values, reaching up to 0.05 ppmv per decade during nighttime.

To investigate the seasonal dependence of ozone trends, we applied a two-step multiple regression technique like that described by Szelag et al. (2020). In the first step, natural cycles (solar, QBO, and ENSO) were estimated and removed from the data using the traditional MLR formulation given above (Eq. 8). The regression was performed using data from each (three-month) season separately. In the second step, the residual time series (after removal of natural variability) was

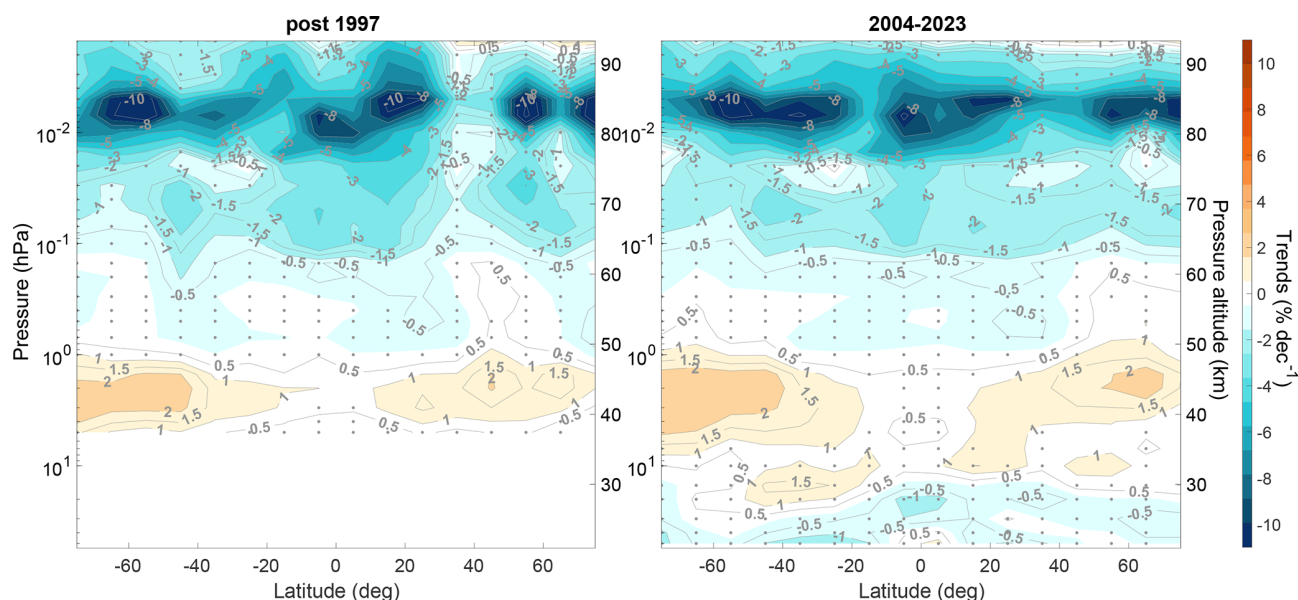


Figure 11. Latitude-altitude variation of ozone trends derived from the METEOR-O3 dataset. The left panel shows trends for 1997–2023, and the right panel shows trends for 2004–2023. The black dots indicate trends that are not statistically significant at the 95 % confidence level. Trends are given in % per decade.

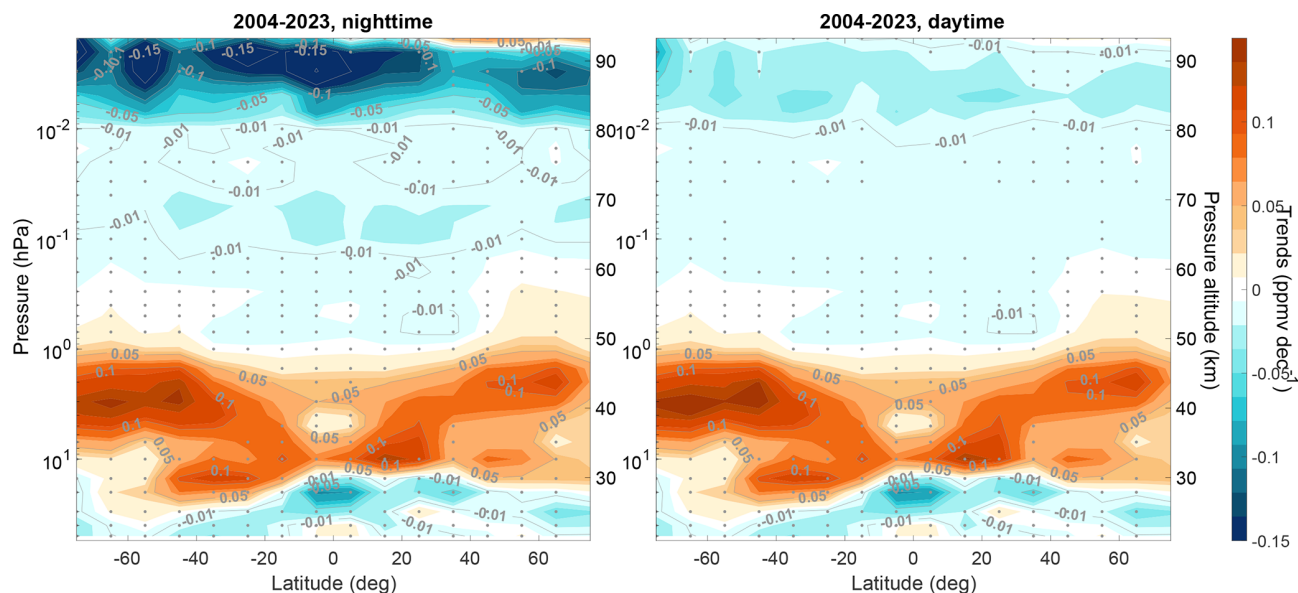


Figure 12. Latitude-altitude variation of ozone trends derived from the METEOR-O3 dataset. Trends are calculated over 2004–2023 for night (left panel) and day (right panel). The black dots denote trends that are not statistically significant at the 95 % confidence level. Trends are given in ppmv per decade.

used to estimate linear trends for the recovery period (2000–2023) using a simple linear regression. This two-step approach provides a robust estimation of seasonal trends by ensuring sufficient data for detecting natural cycles and by fitting linear trends only within periods where ozone changes are approximately linear.

Variations of ozone trends over the period 2000–2023 for each latitude and altitude are shown for each season separately in Fig. 13. In the upper stratosphere, ozone trends are positive throughout all seasons and across most latitudes, consistent with previous studies (Szélag et al., 2020). The strongest positive trends, up to about 2 %–4 % per decade, are observed at middle and high latitudes.

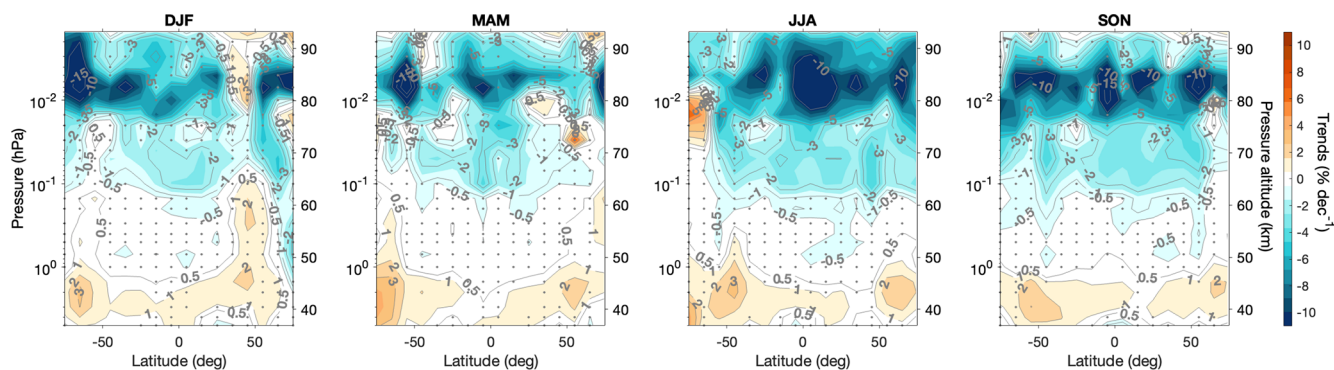


Figure 13. Latitude–altitude distribution of ozone trends derived from the METEOR-O3 dataset for each season (DJF, MAM, JJA, SON) over the period 2000–2023. The black dots denote trends that are not statistically significant at the 95 % confidence level. Trends are given in % per decade.

In the lowermost mesosphere (50–60 km), ozone trends are generally close to zero, with most not statistically significant, suggesting little long-term change in this region. Between approximately 60 and 80 km, negative trends (about -2% to -4% per decade) dominate, indicating a persistent decrease in mesospheric ozone. The largest negative values, reaching up to -15% to -20% per decade, occur between 80 and 90 km, particularly in the Northern Hemisphere during boreal summer (JJA) and in the Southern Hemisphere during austral summer (DJF) where the ozone absolute values are very low. During the equinoctial seasons, negative ozone trends peak at mid-latitudes and in the tropics. In some seasons and latitude bands, however, trends become positive, for example during local winter between 75–80 km and 60–80° latitudes.

7 Summary

We have developed a new merged dataset of middle atmospheric ozone (~ 22 to 100 km), METEOR-O3, constructed from multiple limb emission and occultation satellite instruments (HALOE, MLS, ACE-FTS, MIPAS, GOMOS, and SOFIE). The merging procedure, adapted from previous methods for stratospheric datasets, accounts for the strong diurnal variability of ozone in the mesosphere. The dataset provides monthly zonal-mean ozone anomalies from 1991 to 2023, with 10° latitude resolution and vertical coverage from approximately 22 up to 100 km.

The merged dataset shows excellent internal consistency among datasets and provides robust coverage of the middle and upper atmosphere, with typical uncertainties below 2 % and slightly higher uncertainties (5 %–10 %) near the mesopause. The deseasonalized anomalies derived from METEOR-O3 are well suited for direct use in trend analyses.

Ozone trend evaluation was carried out on pressure levels using two complementary regression methods. The one-step MLR analysis was applied to the full merged dataset (1991–2023) and to the period of best spatio-temporal coverage

(2004–2023). For the full-period analysis, only post-recovery (post-1997) trends were presented. The results show positive trends of about 1% – 2% per decade in the upper stratosphere (35–45 km), consistent with the ongoing ozone recovery observed in earlier studies (Godin-Beekmann et al., 2022; Petropavlovskikh et al., 2019). In the mesosphere, ozone trends are negative, with values of approximately -1% to -3% per decade in the 60–80 km region and up to -8% to -12% per decade between 80 and 90 km. While previous SABER-based studies were temporally and regionally limited (e.g., Bizuneh et al., 2022; Huang et al., 2014), the present analysis extends to a global scale, providing for the first time a comprehensive assessment of long-term mesospheric/lower thermospheric ozone variability.

The METEOR-O3 dataset enables global evaluation of long-term changes and seasonal variations. It offers a valuable resource for model validation and for improving understanding of upper atmospheric processes.

Code and data availability. The merged METEOR-O3 ozone dataset is publicly available from <https://doi.org/10.57707/fmi-b2share.jxst3-8h654> (Szelag and Sofieva, 2026). Updates of the merged dataset will be provided as more recent data become available.

Supplement. The supplement related to this article is available online at <https://doi.org/10.5194/acp-26-7503-2026-supplement>.

Author contributions. MES and VFS designed the study, performed the analyses, prepared illustrations and wrote the manuscript. EM and PTV contributed to the analysis and manuscript design. MLS provided MLS data and data description. MLP, BF, GS and AL provided MIPAS data and data description. KAW and PES provided ACE-FTS data and data description. MEH and BTM provided SOFIE data. The results of the study were dis-

cussed by all co-authors, and all co-authors contributed to writing the paper.

Competing interests. At least one of the (co-)authors is a member of the editorial board of *Atmospheric Chemistry and Physics*. The peer-review process was guided by an independent editor, and the authors also have no other competing interests to declare.

Disclaimer. Publisher's note: Copernicus Publications remains neutral with regard to jurisdictional claims made in the text, published maps, institutional affiliations, or any other geographical representation in this paper. The authors bear the ultimate responsibility for providing appropriate place names. Views expressed in the text are those of the authors and do not necessarily reflect the views of the publisher.

Acknowledgements. The work at Finnish Meteorological Institute has been performed within the framework of the ESA METEOR project (contract 4000145342/24/I-DT-bgh). Work at the Jet Propulsion Laboratory, California Institute of Technology, was carried out under a contract with the National Aeronautics and Space Administration (80NM0018D0004). The IAA team acknowledges financial support from the Agencia Estatal de Investigación, MCIN/AEI/10.13039/501100011033, through grants PID2022-141216NB-I00 and CEX2021-001131-S. MES and VS thank the Research Council of Finland (Flagship of Advanced Mathematics for Sensing Imaging and Modelling, grant 359196).

Financial support. This research has been supported by the European Space Agency (grant no. ESA – 4000145342/24/I-DT-bgh).

Review statement. This paper was edited by John Plane and reviewed by two anonymous referees.

References

- Bailey, S. M., Thurairajah, B., Hervig, M. E., Siskind, D. E., Russell III, J. M., and Gordley, L. L.: Trends in the polar summer mesosphere temperature and pressure altitude from satellite observations, *J. Atmos. Sol.-Terr. Phys.*, 220, 105650, <https://doi.org/10.1016/j.jastp.2021.105650>, 2021.
- Baumgaertner, A. J. G., Seppälä, A., Jöckel, P., and Clilverd, M. A.: Geomagnetic activity related NO_x enhancements and polar surface air temperature variability in a chemistry climate model: modulation of the NAM index, *Atmos. Chem. Phys.*, 11, 4521–4531, <https://doi.org/10.5194/acp-11-4521-2011>, 2011.
- Bernath, P. F.: The Atmospheric Chemistry Experiment (ACE), *J. Quant. Spectrosc. Ra.*, 186, 3–16, <https://doi.org/10.1016/j.jqsrt.2016.04.006>, 2017.
- Bernath, P. F., McElroy, C. T., Abrams, M. C., Boone, C. D., Butler, M., Camy-Peyret, C., Carleer, M., Clerbaux, C., Coheur, P.-F., Colin, R., DeCola, P., DeMazière, M., Drummond, J. R., Dufour, D., Evans, W. F. J., Fast, H., Fussen, D., Gilbert, K., Jennings, D. E., Llewellyn, E. J., Lowe, R. P., Mahieu, E., McConnell, J. C., McHugh, M., McLeod, S. D., Michaud, R., Midwinter, C., Nassar, R., Nichitiu, F., Nowlan, C., Rinsland, C. P., Rochon, Y. J., Rowlands, N., Semeniuk, K., Simon, P., Skelton, R., Sloan, J. J., Soucy, M.-A., Strong, K., Tremblay, P., Turnbull, D., Walker, K. A., Walkty, I., Wardle, D. A., Wehrle, V., Zander, R., and Zou, J.: Atmospheric Chemistry Experiment (ACE): Mission overview, *Geophys. Res. Lett.*, 32, L15S01, <https://doi.org/10.1029/2005GL022386>, 2005.
- Bertaux, J. L., Kyrölä, E., Fussen, D., Hauchecorne, A., Dalaudier, F., Sofieva, V., Tamminen, J., Vanhellefont, F., Fanton d'Andon, O., Barrot, G., Mangin, A., Blanot, L., Lebrun, J. C., Pérot, K., Fehr, T., Saavedra, L., Leppelmeier, G. W., and Friaese, R.: Global ozone monitoring by occultation of stars: an overview of GOMOS measurements on ENVISAT, *Atmos. Chem. Phys.*, 10, 12091–12148, <https://doi.org/10.5194/acp-10-12091-2010>, 2010.
- Bhatt, P. P., Remsberg, E. E., Gordley, L. L., McInerney, J. M., Brackett, V. G., and Russell, J. M.: An evaluation of the quality of Halogen Occultation Experiment ozone profiles in the lower stratosphere, *J. Geophys. Res.-Atmos.*, 104, 9261–9275, <https://doi.org/10.1029/1999JD900058>, 1999.
- Bizuneh, C. L., Jaya Prakash Raju, U., Nigussie, M., and Santos, C. A. G.: Long-term temperature and ozone response to natural drivers in the mesospheric region using 16 years (2005–2020) of TIMED/SABER observation data at 5–15° N, *Adv. Space Res.*, 70, 2095–2111, <https://doi.org/10.1016/j.asr.2022.06.051>, 2022.
- Boone, C. D., Nassar, R., Walker, K. A., Rochon, Y., McLeod, S. D., Rinsland, C. P., and Bernath, P. F.: Retrievals for the atmospheric chemistry experiment Fourier-transform spectrometer, *Appl. Optics*, 44, 7218–7231, <https://doi.org/10.1364/ao.44.007218>, 2005.
- Boone, C. D., Bernath, P. F., and Lecours, M.: Version 5 retrievals for ACE-FTS and ACE-imagers, *J. Quant. Spectrosc. Ra.*, 310, 108749, <https://doi.org/10.1016/j.jqsrt.2023.108749>, 2023.
- Bourassa, A. E., Degenstein, D. A., Randel, W. J., Zawodny, J. M., Kyrölä, E., McLinden, C. A., Sioris, C. E., and Roth, C. Z.: Trends in stratospheric ozone derived from merged SAGE II and Odin-OSIRIS satellite observations, *Atmos. Chem. Phys.*, 14, 6983–6994, <https://doi.org/10.5194/acp-14-6983-2014>, 2014.
- Brasseur, G. P. and Solomon, S.: *Aeronomy of the middle atmosphere*, Springer, Dordrecht, The Netherlands, <https://doi.org/10.1007/1-4020-3824-0>, 2005.
- Cnossen, I.: Analysis and attribution of climate change in the upper atmosphere from 1950 to 2015 simulated by WACCM-X, *J. Geophys. Res.-Space*, 125, <https://doi.org/10.1029/2020ja028623>, 2020.
- Cnossen, I., Emmert, J. T., Garcia, R. R., Elias, A. G., Mlynarczyk, M. G., and Zhang, S.-R.: A review of global long-term changes in the mesosphere, thermosphere and ionosphere: A starting point for inclusion in (semi-) empirical models, *Adv. Space Res.*, 74, 5991–6011, <https://doi.org/10.1016/j.asr.2024.10.005>, 2024.
- Cochrane, D. and Orcutt, G. H.: Application of Least Squares Regression to Relationships Containing Auto-Correlated Error Terms, *J. Am. Stat. Assoc.*, 44, 32–61, <https://doi.org/10.1080/01621459.1949.10483290>, 1949.
- Das, S., Bailey, S. M., Hervig, M. E., Thurairajah, B., and Marshall, B. T.: Validation of Version 1.3 Ozone Measured by

- the SOFIE Instrument, *Earth Space Sci.*, 10, e2022EA002649, <https://doi.org/10.1029/2022EA002649>, 2023.
- Das, U.: Spatial variability in long-term temperature trends in the middle atmosphere from SABER/TIMED observations, *Adv. Space Res.*, 68, 2890–2903, <https://doi.org/10.1016/j.asr.2021.05.014>, 2021.
- Fischer, H., Birk, M., Blom, C., Carli, B., Carlotti, M., von Clarmann, T., Delbouille, L., Dudhia, A., Ehhalt, D., Endemann, M., Flaud, J. M., Gessner, R., Kleinert, A., Koopman, R., Langen, J., López-Puertas, M., Mosner, P., Nett, H., Oelhaf, H., Perron, G., Remedios, J., Ridolfi, M., Stiller, G., and Zander, R.: MIPAS: an instrument for atmospheric and climate research, *Atmos. Chem. Phys.*, 8, 2151–2188, <https://doi.org/10.5194/acp-8-2151-2008>, 2008.
- Godin-Beekmann, S., Azouz, N., Sofieva, V. F., Hubert, D., Petropavlovskikh, I., Effertz, P., Ancellet, G., Degenstein, D. A., Zawada, D., Froidevaux, L., Frith, S., Wild, J., Davis, S., Steinbrecht, W., Leblanc, T., Querel, R., Tourpali, K., Damadeo, R., Maillard Barras, E., Stübi, R., Vigouroux, C., Arosio, C., Nedoluha, G., Boyd, I., Van Malderen, R., Mahieu, E., Smale, D., and Sussmann, R.: Updated trends of the stratospheric ozone vertical distribution in the 60°S–60°N latitude range based on the LOTUS regression model, *Atmos. Chem. Phys.*, 22, 11657–11673, <https://doi.org/10.5194/acp-22-11657-2022>, 2022.
- Gordley, L. L., Burton, J., Marshall, B. T., McHugh, M., Deaver, L., Nelsen, J., Russell, J. M., and Bailey, S.: High precision refraction measurements by solar imaging during occultation: results from SOFIE, *Appl. Optics*, 48, 4814, <https://doi.org/10.1364/AO.48.004814>, 2009a.
- Gordley, L. L., Hervig, M. E., Fish, C., Russell, J. M., Bailey, S., Cook, J., Hansen, S., Shumway, A., Paxton, G., Deaver, L., Marshall, T., Burton, J., Magill, B., Brown, C., Thompson, E., and Kemp, J.: The solar occultation for ice experiment, *J. Atmos. Sol.-Terr. Phys.*, 71, 300–315, <https://doi.org/10.1016/j.jastp.2008.07.012>, 2009b.
- Harris, N. R. P., Kyrö, E., Staehelin, J., Brunner, D., Andersen, S.-B., Godin-Beekmann, S., Dhomse, S., Hadjinicolaou, P., Hansen, G., Isaksen, I., Jrrar, A., Karpetchko, A., Kivi, R., Knudsen, B., Krizan, P., Lastovicka, J., Maeder, J., Orsolini, Y., Pyle, J. A., Rex, M., Vanicek, K., Weber, M., Wohltmann, I., Zanis, P., and Zerefos, C.: Ozone trends at northern mid- and high latitudes – a European perspective, *Ann. Geophys.*, 26, 1207–1220, <https://doi.org/10.5194/angeo-26-1207-2008>, 2008.
- Harris, N. R. P., Hassler, B., Tummon, F., Bodeker, G. E., Hubert, D., Petropavlovskikh, I., Steinbrecht, W., Anderson, J., Bhartia, P. K., Boone, C. D., Bourassa, A., Davis, S. M., Degenstein, D., Delcloo, A., Frith, S. M., Froidevaux, L., Godin-Beekmann, S., Jones, N., Kurylo, M. J., Kyrölä, E., Laine, M., Leblanc, S. T., Lambert, J.-C., Liley, B., Mahieu, E., Maycock, A., de Mazière, M., Parrish, A., Querel, R., Rosenlof, K. H., Roth, C., Sioris, C., Staehelin, J., Stolarski, R. S., Stübi, R., Tamminen, J., Vigouroux, C., Walker, K. A., Wang, H. J., Wild, J., and Zawodny, J. M.: Past changes in the vertical distribution of ozone – Part 3: Analysis and interpretation of trends, *Atmos. Chem. Phys.*, 15, 9965–9982, <https://doi.org/10.5194/acp-15-9965-2015>, 2015.
- Hedin, A. E.: A revised thermospheric model based on mass spectrometer and incoherent scatter data: MSIS-83, *J. Geophys. Res.-Space*, 88, 10170–10188, <https://doi.org/10.1029/JA088iA12p10170>, 1983.
- Hedin, A. E.: Extension of the MSIS thermosphere model into the middle and lower atmosphere, *J. Geophys. Res.-Space Phys.*, 96, 1159–1172, <https://doi.org/10.1029/90JA02125>, 1991.
- Hervig, M. E., Gordley, L. L., Russell III, J. M., and Bailey, S. M.: SOFIE PMC observations during the northern summer of 2007, *J. Atmos. Sol.-Terr. Phys.*, 71, 331–339, <https://doi.org/10.1016/j.jastp.2008.08.010>, 2009a.
- Hervig, M. E., Gordley, L. L., Stevens, M. H., Russell, J. M., III, Bailey, S. M., and Baumgarten, G.: Interpretation of SOFIE PMC measurements: Cloud identification and derivation of mass density, particle shape, and particle size, *J. Atmos. Sol.-Terr. Phys.*, 71, 316–330, <https://doi.org/10.1016/j.jastp.2008.07.009>, 2009b.
- Huang, F. T., Mayr, H. G., Russell III, J. M., and Mlynczak, M. G.: Ozone and temperature decadal trends in the stratosphere, mesosphere and lower thermosphere, based on measurements from SABER on TIMED, *Ann. Geophys.*, 32, 935–949, <https://doi.org/10.5194/angeo-32-935-2014>, 2014.
- Kiefer, M., von Clarmann, T., Funke, B., García-Comas, M., Glatthor, N., Grabowski, U., Höpfner, M., Kellmann, S., Laeng, A., Linden, A., López-Puertas, M., and Stiller, G. P.: Version 8 IMK-IAA MIPAS ozone profiles: nominal observation mode, *Atmos. Meas. Tech.*, 16, 1443–1460, <https://doi.org/10.5194/amt-16-1443-2023>, 2023.
- Kyrölä, E., Tamminen, J., Sofieva, V., Bertaux, J. L., Hauchecorne, A., Dalaudier, F., Fussen, D., Vanhellemont, F., Fanton d’Andon, O., Barrot, G., Guirlet, M., Mangin, A., Blanot, L., Fehr, T., Saavedra de Miguel, L., and Fraisse, R.: Retrieval of atmospheric parameters from GOMOS data, *Atmos. Chem. Phys.*, 10, 11881–11903, <https://doi.org/10.5194/acp-10-11881-2010>, 2010.
- Kyrölä, E., Laine, M., Sofieva, V., Tamminen, J., Päivärinta, S.-M., Tukiainen, S., Zawodny, J., and Thomason, L.: Combined SAGE II–GOMOS ozone profile data set for 1984–2011 and trend analysis of the vertical distribution of ozone, *Atmos. Chem. Phys.*, 13, 10645–10658, <https://doi.org/10.5194/acp-13-10645-2013>, 2013.
- Langematz, U., Grenfell, J. L., Matthes, K., Mieth, P., Kunze, M., Steil, B., and Brühl, C.: Chemical effects in 11-year solar cycle simulations with the Freie Universität Berlin Climate Middle Atmosphere Model with online chemistry (FUB-CMAM-CHEM), *Geophys. Res. Lett.*, 32, L13803, <https://doi.org/10.1029/2005GL022686>, 2005.
- Laštovička, J.: A review of recent progress in trends in the upper atmosphere. *J. Atmos. Solar Terr. Phys.*, 163, 2–13, <https://doi.org/10.1016/j.jastp.2017.03.009>, 2017.
- Laštovička, J.: Progress in investigating long-term trends in the mesosphere, thermosphere, and ionosphere, *Atmos. Chem. Phys.*, 23, 5783–5800, <https://doi.org/10.5194/acp-23-5783-2023>, 2023.
- Laštovička, J., Akmaev, R. A., Beig, G., Bremer, J., and Emmert, J. T.: Global change in the upper atmosphere, *Science*, 314, 1253–1254, <https://doi.org/10.1126/science.1135134>, 2006.
- Li, T., Yue, J., Russell III, J. M., and Zhang, X.: Long-term trend and solar cycle in the middle atmosphere temperature revealed from merged HALOE and SABER datasets, *J. Atmos. Sol.-Terr. Phys.*, 212, 105506, <https://doi.org/10.1016/j.jastp.2020.105506>, 2021.

- Livesey, N. J., Snyder, W. V., Read, W. G., and Wagner, P. A.: Retrieval algorithms for the EOS Microwave Limb Sounder (MLS), *IEEE T. Geosci. Remote Sens.*, 44, 1144–1155, <https://doi.org/10.1109/TGRS.2006.872327>, 2006.
- Livesey, N. J., Read, W. G., Wagner, P. A., Froidevaux, L., Santee, M. L., Schwartz, M. J., Lambert, A., Millán Valle, L. F., Pumphrey, H. C., Manney, G. L., Fuller, R. A., Jarnot, R. F., Brian W. Knosp, B. W., and Lay, R. R.: Version 5.0x Level 2 and 3 data quality and description document, Tech. Rep. No. JPL D-105336 Rev. B, Jet Propulsion Laboratory, <http://mls.jpl.nasa.gov> (last access: 12 May 2026), 2022.
- López-Puertas, M., García-Comas, M., Funke, B., von Clarmann, T., Glatthor, N., Grabowski, U., Kellmann, S., Kiefer, M., Laeng, A., Linden, A., and Stiller, G. P.: MIPAS ozone retrieval version 8: middle-atmosphere measurements, *Atmos. Meas. Tech.*, 16, 5609–5645, <https://doi.org/10.5194/amt-16-5609-2023>, 2023.
- Maliniemi, V., Asikainen, T., and Mursula, K.: Spatial distribution of Northern Hemisphere winter temperatures during different phases of the solar cycle, *J. Geophys. Res.-Atmos.*, 119, 9752–9764, <https://doi.org/10.1002/2013JD021343>, 2014.
- Marsh, D., Smith, A., Brasseur, G., Kaufmann, M., and Grossmann, K.: The existence of a tertiary ozone maximum in the high latitude middle mesosphere, *Geophys. Res. Lett.*, 28, 4531–4534, <https://doi.org/10.1029/2001GL013791>, 2001.
- Marshall, B. T., Deaver, L. E., Thompson, R. E., Gordley, L. L., McHugh, M. J., Hervig, M. E., and Russell III, J. M.: Retrieval of temperature and pressure using broadband solar occultation: SOFIE approach and results, *Atmos. Meas. Tech.*, 4, 893–907, <https://doi.org/10.5194/amt-4-893-2011>, 2011.
- Nath, O. and Sridharan, S.: Long-term variabilities and tendencies in zonal mean TIMED-SABER ozone and temperature in the middle atmosphere at 10–15° N, *J. Atmos. Sol.-Terr. Phys.*, 120, 1–8, <https://doi.org/10.1016/j.jastp.2014.08.010>, 2014.
- Petropavlovskikh, I., Godin-Beekmann, S., Hubert, D., Damadeo, R., Hassler, B., and Sofieva, V.: SPARC/IO3C/GAW report on Long-term Ozone Trends and Uncertainties in the Stratosphere, SPARC/IO3C/GAW, SPARC Report No. 9, WCRP-17/2018, GAW Report No. 241, <https://doi.org/10.17874/f899e57a20b>, 2019.
- Qian, L., Jacobi, C., and McInerney, J. M.: Trends and solar irradiance effects in the mesosphere, *J. Geophys. Res.-Space*, 124, 1343–1360, <https://doi.org/10.1029/2018JA026367>, 2019.
- Qian, L., McInerney, J. M., Solomon, S. S., Liu, H., and Burns, A. G.: Climate changes in the upper atmosphere: Contributions by the changing greenhouse gas concentrations and Earth's magnetic field from the 1960s to 2010s, *J. Geophys. Res.-Space*, 126, <https://doi.org/10.1029/2020ja029067>, 2021.
- Rozanov, E., Callis, L., Schlesinger, M., Yang, F., Andronova, N., and Zubov, V.: Atmospheric response to NO_y source due to energetic electron precipitation, *Geophys. Res. Lett.*, 32, L14811, <https://doi.org/10.1029/2005GL023041>, 2005.
- Rozanov, E., Calisto, M., Egorova, T., Peter, T., and Schmutz, W.: Influence of the Precipitating Energetic Particles on Atmospheric Chemistry and Climate, *Surv. Geophys.*, 33, 483–501, <https://doi.org/10.1007/s10712-012-9192-0>, 2012.
- Russell, J. M., Gordley, L. L., Park, J. H., Drayson, S. R., Hesketh, W. D., Cicerone, R. J., Tuck, A. F., Frederick, J. E., Harries, J. E., and Crutzen, P. J.: The Halogen Occultation Experiment, *J. Geophys. Res.-Atmos.*, 98, 10777–10797, 1993.
- Russell, J. M., Bailey, S. M., Gordley, L. L., Rusch, D. W., Horányi, M., Hervig, M. E., Thomas, G. E., Randall, C. E., Siskind, D. E., Stevens, M. H., Summers, M. E., Taylor, M. J., Englert, C. R., Espy, P. J., McClintock, W. E., and Merkel, A. W.: The Aeronomy of Ice in the Mesosphere (AIM) mission: Overview and early science results, *J. Atmos. Sol.-Terr. Phys.*, 71, 289–299, <https://doi.org/10.1016/j.jastp.2008.08.011>, 2009.
- Salminen, A., Asikainen, T., Maliniemi, V., and Mursula, K.: Effect of energetic electron precipitation on the northern polar vortex: Explaining the QBO modulation via control of meridional circulation, *J. Geophys. Res.-Atmos.*, 124, 5807–5821, <https://doi.org/10.1029/2018JD029296>, 2019.
- Seppälä, A., Randall, C. E., Clilverd, M. A., Rozanov, E., and Rodger, C. J.: Geomagnetic activity and polar surface air temperature variability, *J. Geophys. Res.-Space*, 114, A10312, <https://doi.org/10.1029/2008JA014029>, 2009.
- Seppälä, A., Lu, H., Clilverd, M. A., and Rodger, C. J.: Geomagnetic activity signatures in wintertime stratosphere wind, temperature, and wave response, *J. Geophys. Res.-Atmos.*, 118, 2169–2183, <https://doi.org/10.1002/jgrd.50236>, 2013.
- Seppälä, A., Kalakoski, N., Verronen, P. T., and Szélag, M. E.: Polar mesospheric ozone loss initiates downward coupling of solar signal in the Northern Hemisphere, *Nat. Commun.*, 16, 748, <https://doi.org/10.1038/s41467-025-55966-z>, 2025.
- Sheese, P. E., Boone, C. D., and Walker, K. A.: Detecting physically unrealistic outliers in ACE-FTS atmospheric measurements, *Atmos. Meas. Tech.*, 8, 741–750, <https://doi.org/10.5194/amt-8-741-2015>, 2015.
- Sheese, P. E., Walker, K. A., Boone, C. D., Bourassa, A. E., Degenstein, D. A., Froidevaux, L., McElroy, C. T., Murtagh, D., Russell III, J. M., and Zou, J.: Assessment of the quality of ACE-FTS stratospheric ozone data, *Atmos. Meas. Tech.*, 15, 1233–1249, <https://doi.org/10.5194/amt-15-1233-2022>, 2022.
- Sinnhuber, M., Nieder, H., and Wieters, N.: Energetic Particle Precipitation and the Chemistry of the Mesosphere/Lower Thermosphere, *Surv. Geophys.*, 33, 1281–1334, <https://doi.org/10.1007/s10712-012-9201-3>, 2012.
- Smith, A. K. and Marsh, D. R.: Processes that account for the ozone maximum at the mesopause, *J. Geophys. Res.-Atmos.*, 110, 2005JD006298, <https://doi.org/10.1029/2005JD006298>, 2005.
- Smith, A. K., Harvey, V. L., Mlynczak, M. G., Funke, B., García-Comas, M., Hervig, M., Kaufmann, M., Kyrölä, E., López-Puertas, M., McDade, I., Randall, C. E., Russell, J. M., Sheese, P. E., Shiotani, M., Skinner, W. R., Suzuki, M., and Walker, K. A.: Satellite observations of ozone in the upper mesosphere, *J. Geophys. Res.-Atmos.*, 118, 5803–5821, <https://doi.org/10.1002/jgrd.50445>, 2013.
- Sofieva, V. F., Tamminen, J., Haario, H., Kyrölä, E., and Lehtinen, M.: Ozone profile smoothness as a priori information in the inversion of limb measurements, *Ann. Geophys.*, 22, 3411–3420, <https://doi.org/10.5194/angeo-22-3411-2004>, 2004.
- Sofieva, V. F., Kyrölä, E., Verronen, P. T., Seppälä, A., Tamminen, J., Marsh, D. R., Smith, A. K., Bertaux, J.-L., Hauchecorne, A., Dalaudier, F., Fussen, D., Vanhellefont, F., Fanton d'Andon, O., Barrot, G., Guirlet, M., Fehr, T., and Saavedra, L.: Spatio-temporal observations of the tertiary ozone maximum, *Atmos. Chem. Phys.*, 9, 4439–4445, <https://doi.org/10.5194/acp-9-4439-2009>, 2009.

- Sofieva, V. F., Rahpoe, N., Tamminen, J., Kyrölä, E., Kalakoski, N., Weber, M., Rozanov, A., von Savigny, C., Laeng, A., von Clarmann, T., Stiller, G., Lossow, S., Degenstein, D., Bourassa, A., Adams, C., Roth, C., Lloyd, N., Bernath, P., Hargreaves, R. J., Urban, J., Murtagh, D., Hauchecorne, A., Dalaudier, F., van Roozendaal, M., Kalb, N., and Zehner, C.: Harmonized dataset of ozone profiles from satellite limb and occultation measurements, *Earth Syst. Sci. Data*, 5, 349–363, <https://doi.org/10.5194/essd-5-349-2013>, 2013.
- Sofieva, V. F., Ialongo, I., Hakkarainen, J., Kyrölä, E., Tamminen, J., Laine, M., Hubert, D., Hauchecorne, A., Dalaudier, F., Bertaux, J.-L., Fussen, D., Blanot, L., Barrot, G., and Dehn, A.: Improved GOMOS/Envisat ozone retrievals in the upper troposphere and the lower stratosphere, *Atmos. Meas. Tech.*, 10, 231–246, <https://doi.org/10.5194/amt-10-231-2017>, 2017a.
- Sofieva, V. F., Kyrölä, E., Laine, M., Tamminen, J., Degenstein, D., Bourassa, A., Roth, C., Zawada, D., Weber, M., Rozanov, A., Rahpoe, N., Stiller, G., Laeng, A., von Clarmann, T., Walker, K. A., Sheese, P., Hubert, D., van Roozendaal, M., Zehner, C., Damadeo, R., Zawodny, J., Kramarova, N., and Bhartia, P. K.: Merged SAGE II, Ozone_cci and OMPS ozone profile dataset and evaluation of ozone trends in the stratosphere, *Atmos. Chem. Phys.*, 17, 12533–12552, <https://doi.org/10.5194/acp-17-12533-2017>, 2017b.
- Sofieva, V. F., Szelag, M., Tamminen, J., Arosio, C., Rozanov, A., Weber, M., Degenstein, D., Bourassa, A., Zawada, D., Kiefer, M., Laeng, A., Walker, K. A., Sheese, P., Hubert, D., van Roozendaal, M., Retscher, C., Damadeo, R., and Lumpe, J. D.: Updated merged SAGE-CCI-OMPS+ dataset for the evaluation of ozone trends in the stratosphere, *Atmos. Meas. Tech.*, 16, 1881–1899, <https://doi.org/10.5194/amt-16-1881-2023>, 2023.
- Solomon, S. C., Liu, H.-L., Marsh, D. R., McInerney, J. M., Qian, L., and Vitt, F. M.: Whole atmosphere climate change: Dependence on solar activity, *J. Geophys. Res.-Space*, 124, 3799–3809, <https://doi.org/10.1029/2019JA026678>, 2019.
- Szelag, M. and Sofieva, V. F.: Merged dataset of ozone profiles in the middle atmosphere (METEOR-O3), B2SHARE [data set], <https://doi.org/10.57707/fmi-b2share.jxst3-8h654>, 2026.
- Szelag, M. E., Sofieva, V. F., Degenstein, D., Roth, C., Davis, S., and Froidevaux, L.: Seasonal stratospheric ozone trends over 2000–2018 derived from several merged data sets, *Atmos. Chem. Phys.*, 20, 7035–7047, <https://doi.org/10.5194/acp-20-7035-2020>, 2020.
- Szelag, M. E., Marsh, D. R., Verronen, P. T., Seppälä, A., and Kalakoski, N.: Ozone impact from solar energetic particles cools the polar stratosphere, *Nat. Commun.*, 13, 6883, <https://doi.org/10.1038/s41467-022-34666-y>, 2022.
- Tamminen, J., Kyrölä, E., Sofieva, V. F., Laine, M., Bertaux, J.-L., Hauchecorne, A., Dalaudier, F., Fussen, D., Vanhellefont, F., Fanton-d'Andon, O., Barrot, G., Mangin, A., Guirlet, M., Blanot, L., Fehr, T., Saavedra de Miguel, L., and Fraisse, R.: GOMOS data characterisation and error estimation, *Atmos. Chem. Phys.*, 10, 9505–9519, <https://doi.org/10.5194/acp-10-9505-2010>, 2010.
- von Clarmann, T., Glatthor, N., Grabowski, U., Höpfner, M., Kellmann, S., Kiefer, M., Linden, A., Mengistu Tsidu, G., Milz, M., Steck, T., Stiller, G. P., Wang, D. Y., Fischer, H., Funke, B., Gil-López, S., and López-Puertas, M.: Retrieval of temperature and tangent altitude pointing from limb emission spectra recorded from space by the Michelson Interferometer for Passive Atmospheric Sounding (MIPAS), *J. Geophys. Res.-Atmos.*, 108, 4736, <https://doi.org/10.1029/2003JD003602>, 2003.
- von Clarmann, T., Höpfner, M., Kellmann, S., Linden, A., Chauhan, S., Funke, B., Grabowski, U., Glatthor, N., Kiefer, M., Schieferdecker, T., Stiller, G. P., and Versick, S.: Retrieval of temperature, H₂O, O₃, HNO₃, CH₄, N₂O, ClONO₂ and ClO from MIPAS reduced resolution nominal mode limb emission measurements, *Atmos. Meas. Tech.*, 2, 159–175, <https://doi.org/10.5194/amt-2-159-2009>, 2009.
- Waters, J. W., Froidevaux, L., Harwood, R. S., Jarnot, R. F., Pickert, H. M., Read, W. G., Siegel, P. H., Cofield, R. E., Filipiak, M. J., Flower, D. A., Holden, J. R., Lau, G. K., Livesey, N. J., Manney, G. L., Pumphrey, H. C., Santee, M. L., Wu, D. L., Cuddy, D. T., Lay, R. R., Loo, M. S., Perun, V. S., Schwartz, M. J., Stek, P. C., Thurstans, R. P., Boyles, M. A., Chandra, K. M., Chavez, M. C., Chen, G.-S., Chudasama, B. V., Dodge, R., Fuller, R. A., Girard, M. A., Jiang, J. H., Jiang, Y., Knosp, B. W., LaBelle, R. C., Lam, J. C., Lee, K. A., Miller, D., Oswald, J. E., Patel, N. C., Pukala, D. M., Quintero, O., Scaff, D. M., Van Snyder, W., Tope, M. C., Wagner, P. A., and Walch, M. J.: The Earth Observing System Microwave Limb Sounder (EOS MLS) on the Aura satellite, *IEEE T. Geosci. Remote*, 44, 1075–1092, <https://doi.org/10.1109/TGRS.2006.873771>, 2006.
- Wilhelm, S., Stober, G., and Brown, P.: Climatologies and long-term changes in mesospheric wind and wave measurements based on radar observations at high and mid latitudes, *Ann. Geophys.*, 37, 851–875, <https://doi.org/10.5194/angeo-37-851-2019>, 2019.
- Yuan, T., Solomon, S. C., She, C.-Y., Krueger, D. A., and Liu, H.-L.: The long-term trends of nocturnal mesopause temperature and altitude revealed by Na lidar observations between 1990 and 2018 at midlatitude, *J. Geophys. Res.-Atmos.*, 124, 5970–5980, <https://doi.org/10.1029/2018JD029828>, 2019.